

Chapter 1

Nanointelligence: Information Physics

Fundamentals for Nanophotonics

Makoto Naruse, Naoya Tate, Masashi Aono and Motoichi Ohtsu

Abstract Nanophotonics has been extensively studied with the aim of unveiling and exploiting light-matter interactions that occur at a scale below the diffraction limit of light. From the viewpoint of information, novel architectures, novel design and analysis principles, and even novel computing paradigms should be considered so that we can fully benefit from the potential of nanophotonics for various applications. In this chapter, we first present some fundamental and emergent attributes associated with optical excitation transfer mediated by optical near-field interactions. Toward achieving a computing paradigm that surpasses the classical von Neumann architecture, we describe stochastic solution searching, which exploits the spatiotemporal dynamics of optical excitation transfer. Second, we show information security applications based on near-field applications, together with their theoretical and experimental foundations. Finally, we present a stochastic analysis of light-assisted self-organized material formation in order to gain a deeper understanding of the underlying physics. We consider that a common feature across all of these demonstrations is the extraction of “intelligent” functions and behaviors from an information-based standpoint—an idea represented by the title of this chapter, “*nanointelligence*”.

M. Naruse (✉)

Photonic Network Research Institute, National Institute of Information and Communications Technology, 4-2-1 Nukui-kita, Koganei, Tokyo 184-8795, Japan
e-mail: naruse@nict.go.jp

N. Tate · M. Ohtsu

Department of Electrical Engineering and Information Systems and Nanophotonics Research Center, Graduate School of Engineering, The University of Tokyo, 2-11-16 Yayoi, Bunkyo-ku, Tokyo 113-8656, Japan

M. Aono

Earth-Life Science Institute, Tokyo Institute of Technology, 201202 Ookayama, Meguro-ku, Tokyo 152-8550, Japan
e-mail: masashi.aono@elsi.jp

1.1 Introduction

Light plays a crucial role in information devices and systems in a range of fields, for example, communication, information processing, imaging, and displays. There is no doubt that the superior physical attributes of light constitute the foundations of the benefits for which we are greatly indebted today. At the same time, however, ever increasing quantitative demands, such as the massive amount of digital information carried on networks, necessitate further advancements in optics and photonics. In addition, there has also been a surge in demand for qualitatively novel technologies, such as energy saving [1], mobile and ubiquitous devices [2], solid-state lighting and displays, healthcare and welfare, and safety and security [3, 4], to name a few. Conventional optics and photonics, however, suffer from difficulties in resolving these quantitative and qualitative challenges due to their fundamental limitations, principally, the diffraction limit of light [5].

Nanophotonics, which makes use of interactions between light and matter at a scale below the wavelength of light, has advanced remarkably [6, 7]. An optical near-field, which is localized in the vicinity of nanostructured matter, is free of the diffraction effects imposed on propagating light, in a sense breaking through the diffraction limit, which allows the physical extent of light itself to be reduced [8, 9]. Furthermore, the nature of photons on the nanometer scale, including higher-order atom–light interactions [10], has led to the discovery of unique phenomena observed only on the nanoscale, revealing a physical picture of “dressed photons”, or photons dressed by material excitations [11, 12]. Thus, not only does nanophotonics possess the ability to break through the diffraction limit, but it also allows physical processes that are unachievable conventionally, such as dipole-forbidden transitions. These novel optical near-field processes have led to various devices that have been experimentally demonstrated recently, including light concentration [13], infrared-to-visible light conversion [14], silicon light emission [15, 16], solar cells [17], and so forth. The rapid progress of experimental technologies has been a driving force behind the advances in nanophotonics; ultrafast spectroscopy for nanostructures [18], and size- and position-controlled quantum nanostructures, such as InAs [19], ZnO [20], and shape-engineered nanostructures [21–23], among others.

From the viewpoint of information or system design, on the other hand, there are many unresolved, important basic issues in nanophotonics. For example, system architectures, basic structures for achieving versatile functions, modeling, design, and analysis principles and methods that inherit the physical principles of nanophotonics should be developed. This chapter sheds light on some system-level fundamentals and insights in nanophotonics, with particular focus on achieving “*intelligent*” functions, what we summarize as the concept called “*nanointelligence*”.

It should be emphasized that replacing or competing with conventional computing and information technologies is not necessarily the primary motivation. What should be pursued is to exploit and maximize the potential of the unique physical attributes inherent in nanophotonics. Nanophotonic security, discussed in Sect. 1.3, is one example application where accessibility via light is essential, and optical

near-field processes provide unique solutions [3]. Furthermore, insights gained in the modeling and analysis of nanophotonics are applicable to a wide range of applications besides computing or information processing. They can also contribute to design and analysis in energy applications [24] and nanofabrication [25]. Dwyer et al. have been developing a nano-optical computer architecture for medical and health-care applications based on resonant energy transfer made possible by DNA-based self-assembly [26, 27]. Catrysse et al. have investigated nanostructures for imaging applications [28], where light–matter interactions are essentially and inevitably present, and the unique nanophotonic solutions offered are valuable. Furthermore, system-oriented approaches are beneficial in investigating material formation. Stochastic modeling and analysis in optical-near-field-assisted nanofabrication, which will be dealt with in Sect. 1.4, are typical examples. In more general contexts, dealing with light and matter in a nonequilibrium open system [29] would provide new knowledge in nanophotonics too, as in other fields. Self-organized criticality [30], observed in some nanophotonic experiments [31, 32], is a natural emergent property thanks to the inclusion of energy flow in addition to elemental near-field interactions.

Summing up all of these related aspects, that is to say, a system-oriented approach, or an approach toward realizing intelligent functions, this chapter reviews nanophotonics from an information physics approach, in particular, by examining the three aspects described below.

Optical Excitation Transfer to Go Beyond the von Neumann Architecture

In Sect. 1.2, we deal with localized optical excitation transfer. Conventionally, propagating light is assumed to interact with nanostructured matter in a spatially uniform manner—a principle referred to as the long-wavelength approximation—from which state transition rules are derived, including dipole-forbidden transitions. However, such an approximation is not valid in the case of a localized optical near-field in the vicinity of nanostructured matter; the inhomogeneity of localized light makes even conventionally dipole-forbidden transitions allowable [5]. We will first review some basic and unique attributes of optical excitation transfer from space-, time-, and energy-related perspectives, followed by a stochastic solution search, which will pave the way to a new computing paradigm beyond von Neumann architecture.

Nanophotonics for Security

Section 1.3 deals with security applications of nanophotonics. Optics has been applied in a variety of security applications [4]. However, since the fundamental physical principle usually involves optical far-fields, diffraction of light causes severe difficulties in device scaling and system integration, for example. Nanophotonics can break through the diffraction limit of conventional light and can provide additional functions, such as adding hidden information that is only retrievable via optical near-fields. Section 1.3 first characterizes one fundamental security feature via a rigorous nano-optical theory based on an angular-spectrum representation of electromagnetic fields on the nanoscale. Its applications to information hiding and authentication functions based on shape-engineering of nanostructures are demonstrated. The study will contribute to tamper-resistant hardware based on unique nano-optical physical processes available on the nanoscale.

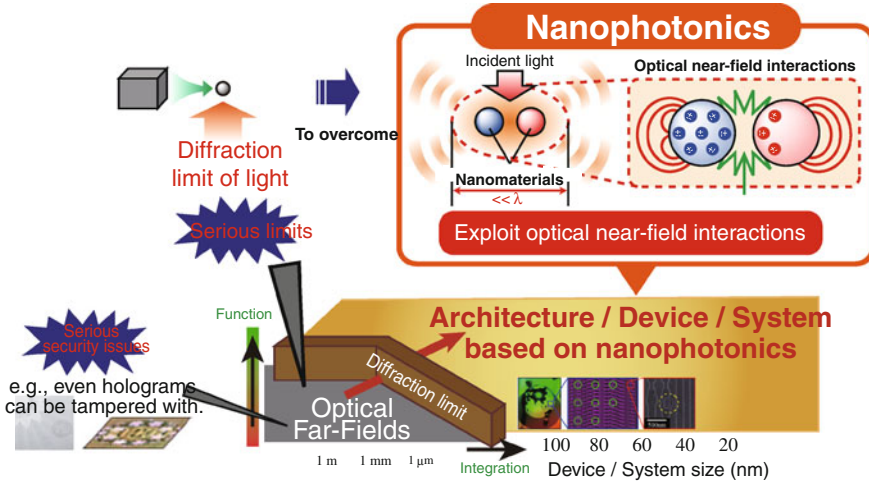


Fig. 1.1 Overall concept of the discussion presented in this chapter

Stochastic Modeling of Near-Field Processes for Intelligent Material Formation

Nanofabrication involving optical near-field processes has demonstrated nanoparticle size regulation [33], nanoparticle array formation [34], the appearance of interesting photosensitivity [17], atomic-scale surface flattening [35], etc., where self-organizing, or “*intelligent*”, behavior emerges by introducing light in material formation. Section 1.4 concerns stochastic modeling of material formation involving optical near-field processes that reproduce phenomenological characteristics consistent with the experimental observations, in order to gain a deeper understanding of the underlying physical mechanisms and to enable optimization of future devices.

The above concept is schematically shown in Fig. 1.1. Section 1.5 summarizes this chapter and discusses some future prospects.

1.2 Optical Excitation Transfer to go Beyond the von Neumann Architecture

In this section, we discuss optical excitation transfer involving optical near-field interactions. In the literature, dipole–dipole interactions, such as Förster resonant energy transfer, are typically referred to in explaining energy transfer from smaller quantum dots (QDs) to larger ones [36, 37]. However, it should be noted that such modeling based on point dipoles does not allow optical transitions to dipole-forbidden energy sublevels. Also, recent experimental observations in light harvesting antenna indicate the inaccuracy of dipole-based modeling [38–40]. On the other hand, as discussed below, the localized nature of optical near-fields frees us from conventional optical selection rules, meaning that optical excitations could excite QDs to energy levels

that are conventionally electric-dipole forbidden. Section 1.2.1 reviews the theoretical formalisms of optical excitation transfer. Section 1.2.2 examines some basic and unique attributes provided by optical excitation transfer from space-, time-, and energy-related perspectives. Section 1.2.3 discusses stochastic solution searching, paving the way to a new computing paradigm beyond the classical von Neumann architecture.

1.2.1 Fundamentals

We begin with the interaction Hamiltonian between an electron–hole pair and an electric field, which is given by

$$\hat{H}_{int} = - \int d^3r \sum_{i, j=e, h} \hat{\psi}_i^\dagger(\mathbf{r}) e\mathbf{r} \cdot \mathbf{E}(\mathbf{r}) \hat{\psi}_j(\mathbf{r}), \quad (1.1)$$

where e represents the electron charge, $\hat{\psi}_i^\dagger(\mathbf{r})$ and $\hat{\psi}_j(\mathbf{r})$ are respectively creation and annihilation operators of either an electron ($i, j = e$) or a hole ($i, j = h$) at position \mathbf{r} , and $\mathbf{E}(\mathbf{r})$ is the electric field [24]. In usual light–matter interactions, $\mathbf{E}(\mathbf{r})$ is a constant since the electric field of propagating light is homogeneous on the nanometer scale. Therefore, we can derive optical selection rules by calculating the dipole transition matrix elements. As a consequence, in the case of spherical quantum dots, for instance, only transitions to states specified by $l = m = 0$ are allowed, where l and m are the orbital angular momentum quantum number and magnetic quantum number, respectively. In the case of optical near-field interactions, on the other hand, due to the large spatial inhomogeneity of the localized optical near-fields at the surface of nano-scale material, an optical transition that violates conventional optical selection rules is allowed. Detailed theory can be found in [12].

Here we assume two spherical quantum dots whose radii are R_S and R_L , which we call QD_S and QD_L , respectively, as shown in Fig. 1.2a. The energy eigenvalues of states specified by quantum numbers (n, l) are given by

$$E_{nl} = E_g + E_{ex} + \frac{\hbar^2 \alpha_{nl}^2}{2MR^2} \quad (n = 1, 2, 3, \dots), \quad (1.2)$$

where E_g is the band gap energy of the bulk semiconductor, E_{ex} is the exciton binding energy in the bulk system, M is the effective mass of the exciton, and α_{nl} are determined from the boundary conditions, for example, as $\alpha_{n0} = n\pi$, $\alpha_{11} = 4.49$. According to (1.2), there exists a resonance between the level of quantum number $(1, 0)$ in QD_S and that of quantum number $(1, 1)$ in QD_L if $R_L/R_S = 4.49/\pi \approx 1.43$. Note that the $(1, 1)$ -level in QD_L is a dipole-forbidden energy level. However, an optical near-field, denoted by U_{SL_2} in Fig. 1.2a, allows this level to be populated due to the steep electric field in the vicinity of QD_S . Therefore, an exciton in the $(1, 0)$ -level in QD_S could be transferred to the $(1, 1)$ -level in QD_L . In QD_L , the excitation

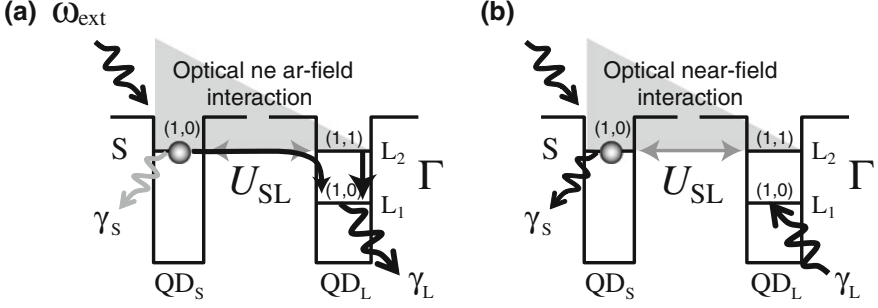


Fig. 1.2 **a** Optical excitation transfer from a smaller quantum dot (QD_S) to a larger one (QD_L) mediated by optical near-field interactions. Note that transition to the energy level L₂ in QD_L is conventionally dipole-forbidden. The energy dissipation occurring at QD_L, or the relaxation from L₂ to L₁, guarantees unidirectionality. **b** State filling induced at the lower energy level in the larger dot results in different flows of optical excitation

undergoes intersublevel energy relaxation due to exciton–phonon coupling, denoted by Γ , which is faster than the near-field interaction [41, 42], and the excitation relaxes to the (1, 0)-level, from where it radiatively decays. Also, since the radiation lifetime of quantum dots is inversely proportional to their volume [43], finally we find unidirectional optical excitation transfer from QD_S to QD_L.

We first introduce quantum mechanical modeling of the total system based on a density matrix formalism. There are in total eight states where either zero, one, or two excitation(s) can sit in the energy levels S, L₁, and L₂ in the system. The interactions between QD_S and QD_L are denoted by U_{SL} , and the radiative relaxation rates from S and L₁ are respectively given by γ_S and γ_L . The model Hamiltonian of the coupled two-dot system is given by

$$H = \hbar \begin{pmatrix} \Omega_S & U_{SL} \\ U_{SL} & \Omega_L \end{pmatrix} \quad (1.3)$$

where $\hbar U_{SL}$ is the optical near-field interaction, and $\hbar \Omega_S$ and $\hbar \Omega_L$ respectively refer to the eigenenergies of QD_S and QD_L. The behavior of optical excitation transfer is obtained by solving the equation of motion, given by the Liouville equation [44]

$$\dot{\rho}(t) = -\frac{i}{\hbar} [H, \rho(t)] - N_\Gamma \rho(t) - \rho(t) N_\Gamma, \quad (1.4)$$

where ρ is the density operator, and N_Γ is a diagonal matrix whose diagonal elements are $\gamma_S/2$ and $\Gamma/2$.

If necessary, we can explicitly include an external Hamiltonian H_{ext} representing the interaction between the external input light at frequency ω_{ext} and the quantum dot system; this is given by

$$H_{ext}(t) = gate(t) \times \left[\left(\exp(i(\Omega_S - \omega_{ext}))S^\dagger + \exp(-i(\Omega_S - \omega_{ext}))S \right) + \left(\exp(i(\Omega_{L_1} - \omega_{ext}))L_1^\dagger + \exp(-i(\Omega_{L_1} - \omega_{ext}))L_1 \right) \right], \quad (1.5)$$

where $gate(t)$ specifies the duration and the amplitude of the external input light, and $S^\dagger(S)$ and $L_1^\dagger(L_1)$ represents creation (annihilation) operators regarding the $(1, 0)$ -levels in QD_S and QD_{L_1} , respectively. If control light occupies the energy level L_1 , namely, state filling is induced at the lower energy level in the larger dot, optical excitation generated at QD_S goes back and forth in the resonant energy level (nutation), resulting in radiation from QD_S (Fig. 1.2b). The following section describes some of the emergent characteristics.

1.2.2 Space-, Time-, and Energy-Related Basic Functions

1.2.2.1 Global Summation Based on Optical Excitation Transfer: A Space-Domain Related Fundamental

The global summation, or data gathering, denoted by $\sum_{i=1}^N x_i$, where x_i represents N binary bits, is an important basic function in a wide range of electrical and optical devices and systems, such as optical code-division multiplexing (OCDM) [45], optical correlators [46], and content addressable memory (CAM) LSI chips [47, 48], among others. In known optical methods, wave propagation in free-space or in waveguides, using focusing lenses or fiber couplers, for example, is well-matched with such a data gathering scheme because the physical nature of propagating light is inherently suitable for the collection or distribution of information. However, the achievable level of integration of these methods is restricted due to the diffraction limit of light. In nanophotonics, on the other hand, the near-field interaction is inherently physically local.

The global data gathering mechanism, or summation, is realized based on the unidirectional energy flow via an optical near-field, as schematically shown in Fig. 1.3a, where surrounding excitations are transferred towards a quantum dot QD_C located at the center through optical near-field interactions [13, 49]. The lowest energy level in each quantum dot is coupled to a free photon bath to sweep out the excitation radiatively. The output signal is proportional to the lowest energy level in QD_C .

An experiment was performed to verify the nanoscale summation using CuCl quantum dots in an NaCl matrix, which has also been employed for demonstrating nanophotonic switches [50] and optical nano-fountains [13]. A quantum dot arrangement in which three small QDs (QD_1 to QD_3) surround a large QD at the center (QD_C) was chosen. Here, at most three light beams with different wavelengths, 325, 376, and 381.3 nm, are radiated to excite the respective quantum dots QD_1 to QD_3 , having sizes of 1, 3.1, and 4.1 nm. The excited excitons are transferred to QD_C , and their radiation is observed by using a near-field fiber probe tip. Notice the output

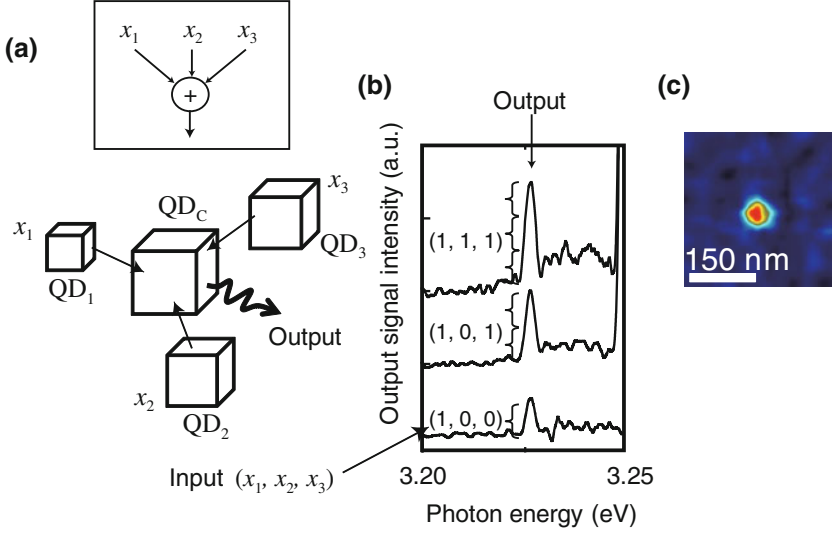


Fig. 1.3 **a** Architecture for global summation by optical excitation transfer. **b** Output signal intensity in frequency domain and **c** space-domain distribution

signal intensity at a photon energy level of 3.225 eV in Fig. 1.3b, which corresponds to a wavelength of 384 nm, or a QD_C size of 5.9 nm. The ratio of the intensities is approximately 1:2:3, depending on the number of excited QDs in the vicinity, as observed in Fig. 1.3b. The spatial intensity distribution was measured by scanning the fiber probe, as shown in Fig. 1.3c, where the energy is converged at the center. Hence, this architecture works as a summation mechanism that counts the number of input channels, based on exciton energy transfer via optical near-field interactions. Also, recently, stacked InAs quantum dots have been used to demonstrate room-temperature optical excitation transfer [51].

1.2.2.2 Optical Pulsation Based on Optical Excitation Transfer: A Time-Domain Related Fundamental

Generating an optical pulse train is one of the most important functionalities required for optical systems. Conventional principles of optical pulse generation are typically based on optical energy build-up in a cavity whose size is much larger than the optical wavelength; thus, the volume and the energy efficiency of the entire system have serious limitations. For nanophotonic applications, novel principles should be developed on the nanometer scale. In fact, Shojiguchi et al. theoretically investigated the possibility of generating superradiance in N two-level systems interacting with optical near-fields [52]. This approach, however, requires precise control of the initial states, which is not straightforward to implement. Here, we theoretically

demonstrate an optical pulsation method based on optical near-field interactions pumped by continuous-wave (CW) light irradiation [53]. With an architecture composed of two subsystems each of which involves excitation transfer based on optical near-field interactions, we observe pulsation in the populations based on a model system using a density matrix formalism. The details are described in [53].

As discussed in Sect. 1.2.1, when the lower level of QD_L is populated by an external input, the optical excitation occurring in QD_S cannot be transferred to QD_L because the lower energy level in QD_L is populated, which is called the state filling effect. Putting it another way, the population of the $(1, 0)$ -level in QD_S is changed by the external input applied to L_1 in QD_L . Optical pulsation based on optical excitation transfer comes from the idea that the externally applied change induced in L_1 can be provided in a self-induced manner by S_1 with a certain timing delay. If QD_S is irradiated with continuous input light, such a change should repeat with a certain period; that is, a pulsed signal should result.

We consider two quantum dot systems, each of which consists of one smaller and one larger QD, as shown in Fig. 1.4a. One system, called *System 1* hereafter, is represented by one smaller dot (QD_C) and one larger dot (QD_G). A CW input is provided to the upper level of QD_C . The optical near-field interaction between QD_C and QD_G is denoted by U_{CG} . Another system, called *System 2*, provides a delay time by multiple use of smaller and larger dots, as already experimentally realized in reference [54]. However, modeling the delay caused by multiple QDs makes the discussion of pulsation mechanisms unnecessarily complicated; thus, we assume an arbitrary delay time applied to the input signal of System 2, denoted by Δ , followed by the last two quantum dots in the delay system, namely, a smaller QD (QD_A) and a larger QD (QD_B), as indicated in Fig. 1.4a. Here, QD_A accepts radiation from QD_C in System 1; that is, the change of the states in QD_C is transferred to QD_A . The optical near-field interaction between QD_A and QD_B is denoted by U_{AB} . The output from QD_B then influences the lower energy level of QD_G .

We described the details of the above modeling based on a density matrix formalism. For example, regarding System 1, there are in total three energy levels (namely, C_1 in QD_C , and G_1 and G_2 in QD_G). The radiative relaxation rates from C_1 and G_1 are respectively given by γ_C and γ_G . Then we rigorously derived the quantum master equations for System 1 and System 2, respectively [53].

We assume the following typical parameter values based on experimental observations of energy transfer observed in ZnO quantum dots [55]: inter-dot optical near-field interactions (144 ps), sublevel relaxation (10 ps), and radiative decay times of the smaller dot (443 ps) and the large dot (190 ps). Also, we assume 1 ns for the delay Δ in System 2. Figure 1.4b demonstrates an example of the evolution of the populations involving the lower level of QD_G (G_1) for different CW input light amplitudes, where optical pulsation is successfully observed with appropriate input light amplitudes, as summarized by the peak-to-peak population of the pulsations shown in Fig. 1.4c. The detailed parameter dependencies were discussed in [53], validating the importance of optical excitation transfer.

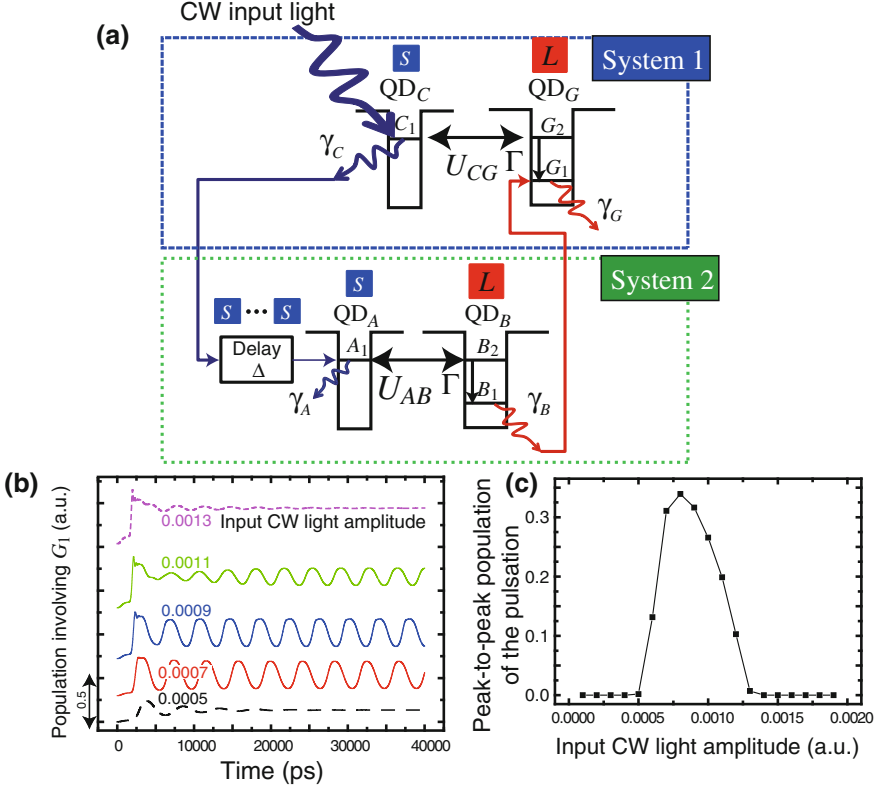


Fig. 1.4 **a** System architecture of pulsation composed of two subsystems each of which provides optical excitation transfer from QD_S to QD_L . **b** Evolution of population in the lower energy level of QD_G with different CW input light amplitudes. **c** Peak-to-peak population of pulsation versus input CW light amplitude

1.2.2.3 Energy Efficiency

We now discuss the lower bound of energy dissipation required for an optical excitation transfer by introducing two representative systems (System A and System B) [56]. The first one, System A in Fig. 1.5a, consists of two closely located quantum dots, and thus, optical excitation transfer from QD_S to QD_L occurs. We assume an interaction time U_{SL}^{-1} of 100 ps for System A, denoted by $U_A^{-1} = 100$ ps in Fig. 1.5a. Such an interaction time is close to that of experimentally observed optical near-field interactions in CuCl QDs (130 ps) [50], ZnO quantum-well structures (130 ps) [20], ZnO QDs (144 ps) [55], and CdSe QDs (135 ps) [54]. The intersublevel relaxation time due to exciton–phonon coupling is in the 1–10 ps range [41, 42, 57], and here we assume $\Gamma^{-1} = 10$ ps. In System B on the other hand (Fig. 1.5a), the two quantum dots are intentionally located far away from each other. Therefore, the interactions between QD_S and QD_L should be negligible, and thus, optical excitation transfer

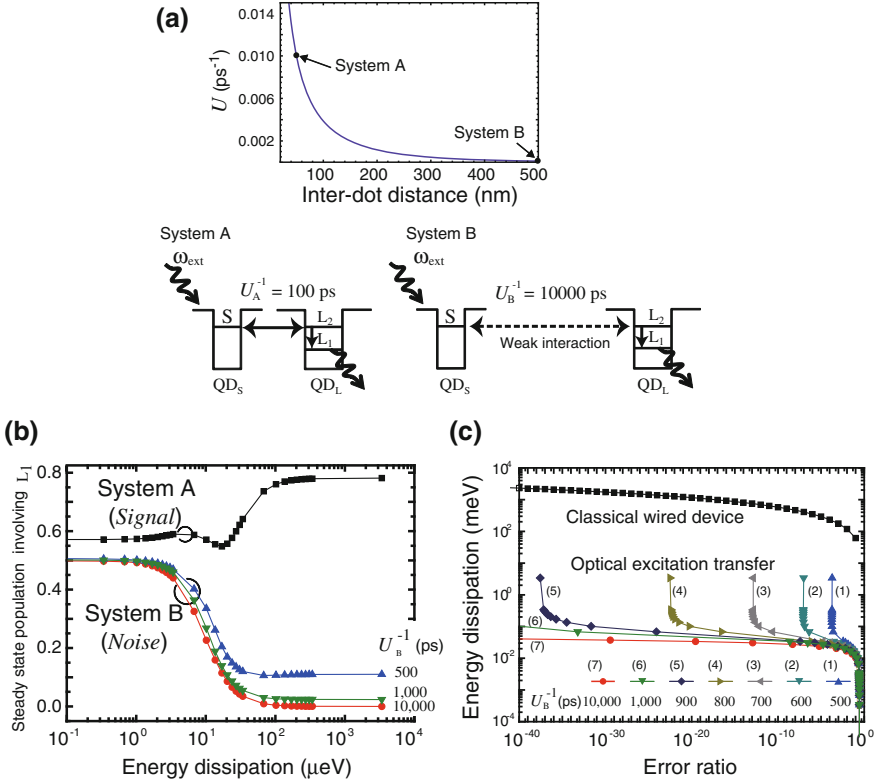


Fig. 1.5 Energy efficiency of optical excitation transfer. **a** Yukawa-type screened potential of an optical near-field interaction between two QDs as a function of the inter-dot distance. We assume two systems consisting of a small QD (QD_S) and a large QD (QD_L): System A has a strong inter-dot near-field interactions (100 ps), whereas System B has negligible interaction (10,000 ps). **b** Steady-state population involving energy level L_1 in System A (squares) and System B as a function of the energy dissipation. For System B, three different cases are shown, with U_B^{-1} of 500, 1,000, and 10,000 ps, respectively indicated by, and marks. **c** Energy dissipation as a function of error ratio regarding optical excitation transfer and the bit flip energy required in a CMOS logic gate. The energy dissipation of optical excitation transfer is about 10^4 -times lower than that in classical electrically wired devices.

from QD_S to QD_L should not occur; namely, the radiation from QD_L should normally be zero. We assume $U_{SL}^{-1} = 10,000$ ps for System B, denoted by U_B^{-1} in Fig. 1.5a, indicating effectively no interactions between the two.

One remark here is that the inter-dot interaction times of System A and System B are related to the distances between the two quantum dots. The optical near-field interaction between two nanoparticles is known to be expressed as a screened potential using a Yukawa function, given by

$$U = \frac{A \exp(-\mu r)}{r}, \quad (1.6)$$

where r is the distance between the two [58]. In this representation, the optical near-field is localized around nanoparticles, and its decay length is equivalent to the particle size. Here, it should be noted that the inter-dot distance of System B indicates how close independent functional elements can be located. In other words, the interaction time of System B is correlated with the integration density of the total system. In order to analyze such spatial density dependencies, we assume that the U_{SL}^{-1} values of 100 and 10,000 ps respectively correspond to inter-dot distances of 50 and 500 nm. Here, the stronger interaction (100 ps) has been assumed, as already mentioned, based on a typical interaction time between closely spaced quantum dots. We also assume that the interaction with negligible magnitude (10,000 ps) corresponds to a situation where the inter-dot distance is close to the optical wavelength. Figure 1.5a shows the Yukawa-type potential curve given by (1.6).

When we assume a longer duration of the input light, the population converges to a steady state. When a pulse with a duration of 10 ns at the same wavelength (365 nm) is radiated, Fig. 1.5b summarizes the steady state output populations involving energy level L_1 evaluated at $t = 10$ ns as a function of the energy dissipation. The intended system behavior, that is, a higher output population in System A and a lower one in System B, is obtained in the region where the energy dissipation is larger than around $25 \mu\text{eV}$. If we treat the population in System A as the amplitude of a “signal” and that in System B as “noise”, the signal-to-noise ratio (SNR) can be evaluated based on the numerical values in Fig. 1.5b. To put it another way, from the viewpoint of the destination QD (or QD_L), the signal should come from a QD_S in its proximity (as in the case of System A), not from a QD_S far from QD_L (as in the case of System B); such a picture will aid in understanding the physical meaning of the SNR defined here. Also, here we assume that the input data are coded in an external system, and that QD_S is irradiated with input light at frequency ω_{ext} . With the SNR, the error ratio (P_E), or equivalently the bit error rate (BER), is derived by the formula $P_E = (1/2)\text{erfc}(\sqrt{\text{SNR}}/2\sqrt{2})$ where $\text{erfc}(x) = 2/\sqrt{\pi} \int_x^\infty \exp(-x^2)dx$, called the complementary error function [59]. The circles in Fig. 1.5c represent the energy dissipation as a function of the error ratio assuming the photon energy used in the above study (3.4 eV). According to [60], the minimum energy dissipation (E_d) in classical electrically wired devices (specifically, the energy dissipation required for a single bit flip in a CMOS logic gate) is given by $E_d = k_B T \ln(\sqrt{3}P_E/2)$, which is indicated by the squares in Fig. 1.5c. For example, when the error ratio is 10^{-6} , the minimum Δ in the optical excitation transfer is about 0.024 meV, whereas that of the classical electrical device is about 303 meV; the former is about 10^4 times more energy efficient than the latter.

As mentioned earlier, the performance of System B depends on the distance between the QDs. When the interaction time of System B (U_B^{-1}) increases, such as 500 ps, the steady state population involving L_1 is as indicated by the triangular marks in Fig. 1.5b; the population stays higher even with increasing energy dissipation

compared with the former case of $U_B^{-1} = 10,000$ ps. This means that the lower bound of the SNR results in a poorer value. In fact, as demonstrated by the triangular marks (1) in Fig. 1.5c, the BER cannot be smaller than around 10^{-4} , even with increasing energy dissipation. The lower bound of the BER decreases as the interaction time U_B^{-1} increases (namely, weaker inter-dot interaction), as demonstrated by the triangular and square marks (2) to (6) in Fig. 1.5c.

Finally, here we make a few remarks regarding the discussion above. First, we assumed arrays of identical independent circuits in the above discussion of density. Therefore, two circuits need spatial separations given by U_B so that unintended behavior does not occur. However, when two adjacent nanophotonic circuits are operated with different optical frequencies so that they can behave independently [61], those two circuits could be located closer together, which would greatly improve the integration density as a whole. Further analysis and design methodologies of complex nanophotonic systems, as well as comparison to electronic devices, is another topic to be pursued in future work. Second, because the energy separation in a single destination QD is limited by its size and lies in the range of meV, the results for energy separations in the μeV range correspond to cases where the destination dot QD_L represents a theoretical model of a coupled quantum dot system such as a pair of quantum dots. The coupled system exhibits optical near-field interactions with the smaller QD, followed by inter-dot electron transfer resulting in optical radiation. In fact, Matsumoto et al. have demonstrated spin-dependent carrier transfer leading to optical radiation between a coupled double quantum well system composed of magnetic and nonmagnetic semiconductors [62], which can be applied to quantum dot systems [63]. Third, a discussion of input and output interfaces is necessary. The above discussion has focused on the lower bound of energy dissipation in the quantum dots. Practical operation of real devices requires input and output interfaces, and the minimum number of photons for a bit slot may be of concern when taking account of noise at the receivers. In [64], Naruse et al. unified such considerations into an evaluation model and analyzed experimental results based on stacked QDs [19]. It was found that optical excitation transfer still exhibits around 10^4 -times better energy efficiency compared with electronic counterparts [64].

1.2.3 Going Beyond the von Neumann Architecture: Stochastic Solution Searching

Another aspect of the stochastic nature inherent in nanophotonics is its application to novel computing devices and architectures [65]. Nature-inspired architectures are attracting significant attention in various research arenas, such computational neurosciences, stochastic-based computing and noise-based logic, and spatiotemporal computation dynamics [66], in order to benefit from the superior attributes of nature and living systems.

Among this research, Aono et al. demonstrated “amoeba-based computing” tasks, such as solving the constraint satisfaction problem (CSP) [66] and the traveling

salesman problem (TSP) [67], by utilizing the spatio-temporal oscillatory dynamics of the photoresponsive amoeboid organism *Physarum* combined with external optical feedback control. These demonstrations indicate that spatiotemporal stochastic dynamics can be utilized for obtaining solutions for problems which today's von Neumann-architecture computers cannot deal with efficiently. In particular, it should be noted that the optical excitation transfer between quantum nanostructures mediated by optical near-field interactions is fundamentally probabilistic, as indicated by the quantum master equations. Until energy dissipation is induced, an optical excitation simultaneously interacts with all potentially transferable destination quantum dots in the resonant energy level. Such a probabilistic behavior can be used for solution searching and exploration. In addition, the optical energy transfer has been shown to be 10^4 -times more energy efficient than that of the bit-flip energy required in conventional electrically wired devices, as discussed in Sect. 1.2.2.3 [56].

Here, we investigate the spatiotemporal dynamics inherent in optical excitation transfer. Furthermore, we demonstrate that it can be utilized for solving a CSP. The optical excitation transfer depends on the existence of resonant energy levels between the quantum dots (QDs) or the state filling effect occurring at the destination QDs. Such a spatial and temporal mechanism yields different evolutions of energy transfer patterns combined with certain feedback mechanisms. In contrast to biological substrates, optical energy transfer is implemented by highly-controlled engineering means for designated structures. The operating speed of such optical near field-mediated QD systems, which is on order of nanoseconds when we are concerned with radiative relaxation processes, is also significantly faster than ones based on biological organisms, which is on the order of seconds or minutes [66].

In addition, we should emphasize that the concept and the principles discussed here are fundamentally different from those of conventional optical computing or optical signal processing, which are limited by the abilities of propagating light. The concept and the principles are also different from the quantum computing paradigm where the superposition of all possible states is exploited to lead to a correct solution. The optical near field-mediated energy transfer is a coherent process, indicating that an optical excitation could be transferred to all possible destination QDs via a resonant energy level, but such coherent interaction between QDs results in a unidirectional energy transfer by means of an energy dissipation process occurring in the larger dot. Thus, our approach paves the way to another computing paradigm in which both coherent and dissipative processes are exploited.

Here we assume one smaller quantum dot, denoted by QD_S , and four larger quantum dots, denoted by QD_{L1} , QD_{L2} , QD_{L3} , and QD_{L4} , as shown in Fig. 1.6a. The smaller and larger QDs are resonant with each other. Figure 1.6b shows representative parameterizations associated with the system; for example, the (1, 0)-level in the smaller QD is denoted by S, and the (1,1)-level in QD_{L_i} is denoted by $L_i^{(U)}$. These levels are resonant with each other and are connected by inter-dot interactions denoted by U_{SL_i} ($i = 1, \dots, 4$). The lower level in QD_{L_i} , namely, the (1, 0)-level, is denoted by $L_i^{(L)}$, which could be filled via the sublevel relaxation from $L_i^{(U)}$ denoted by Γ_{L_i} . The radiations from the S and L_i levels are respectively represented by the relaxation

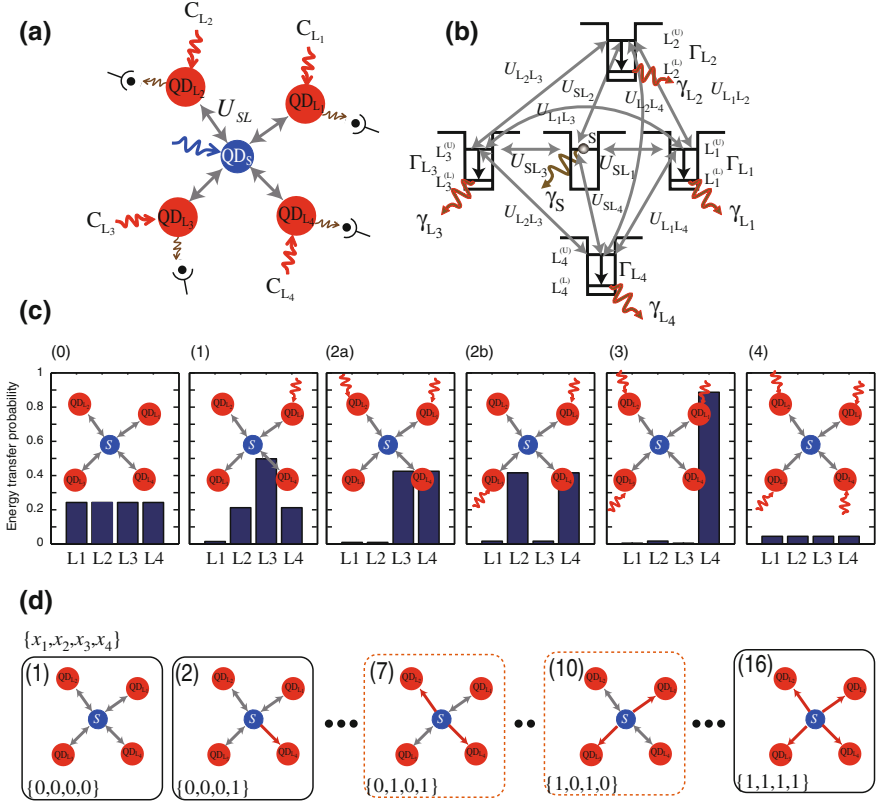


Fig. 1.6 **a** Architecture of the optical-energy-transfer-based system for solving constraint satisfaction problem and composed of a smaller quantum dot and four larger quantum dots **b** and its energy diagram. Radiation from the larger quantum dots is detected. Control light is used for inducing state filling in the larger quantum dots. **c** Energy transfer probabilities calculated as time integrals of the populations depending on the state filling of the larger dots, shown in (a). There are a total of six different spatial arrangements of the induced state filling, excluding the symmetries. **d** There are a total of $2^4 (=16)$ different combinations of binary values in the given problem. The correct solutions are the state numbers (7) and (10), where $\{x_1, x_2, x_3, x_4\}$ are respectively given by $\{0, 1, 0, 1\}$ and $\{1, 0, 1, 0\}$

constants γ_S and γ_{L_i} . We call the inverse of those relaxation constants the radiation lifetime in the following. We also assume that the photon radiated from the lower level of QD_{L_i} can be separately captured by photodetectors. The channels of control light, denoted by C_{L_i}, can induce a state filling effect at L_i^(L). Summing up, Fig. 1.6a schematically represents the architecture of the system to be studied in this section for solving a CSP.

In the numerical calculation, we assume $U_{SL_i}^{-1} = 100$ ps, $\Gamma_i^{-1} = 10$ ps, $\gamma_{L_i}^{-1} = 1$ ns, and $\gamma_S^{-1} = 2.92$ ns as a typical parameter set. If there is no state filling in the system, an optical excitation sitting initially at S can be transferred to any one of QD_{L₁} to

QD_{L4} with the same probability, as demonstrated in Fig. 1.6c, 0, which is the time-integral of the population involving the energy level $L_i^{(L)}$. If QD_{L1} suffers from state filling, on the other hand, the initial excitation at S is more likely to be transferred to QD_{L2} , QD_{L3} , or QD_{L4} , as shown in Fig. 1.6c, 1. Looking at the results more closely, the probability of transfer to QD_{L3} is higher than the probabilities of transfer to QD_{L2} and QD_{L4} by considering the geometrical arrangements of the system. A detailed discussion is found in [65]. Additionally, the energy transfer probabilities in the presence of two-, three-, or four-state filling are summarized in Fig. 1.6c. The energy transfer probability, given by the integral of the population divided by a constant gain factor, is a figure-of-merit (FoM) indicating the trend of optical energy transfer from the smaller quantum dot to the four larger ones. This energy transfer probability does *not* obey the conservation law of probability, namely, the summation of the transition probabilities to QD_{L_i} is not unity. Instead, we see that the energy transfer to QD_{L_i} occurs if a random number generated uniformly between 0 and 1 is less than the transition probability to QD_{L_i} .

The idea for problem solving is to control optical energy transfer by controlling the destination QD by using control light in an adequate feedback mechanism. We assume that photon radiation, or observation, from the energy level $L_i^{(L)}$ is equivalent to a binary value x_i resulting in a logical 1 level, whereas no observation of a photon means $x_i = 0$.

We consider the following constraint satisfaction problem as an example regarding an array of N binary-valued variables $x_i (i = 1, \dots, N)$. The constraint is that $x_i = NOR(x_{i-1}, x_{i+1})$ should be satisfied for all i . That is, variable x_i should be consistent with a logical NOR operation of the two neighbors. For $i = 0$ and N , the constraints are respectively given by $x_1 = NOR(x_N, x_2)$ and $x_N = NOR(x_{N-1}, x_1)$. We call this problem the “NOR problem” in the following. Taking account of the nature of an individual NOR logic operation, one important inherent character is that if $x_i = 1$ then its two neighbors should both be zero, or $x_{i-1} = x_{i+1} = 0$. Recall that a photon radiated, or observed, from the energy level $L_i^{(L)}$ corresponds to a binary value $x_i = 1$, whereas the absence of an observed photon means $x_i = 0$. Therefore, $x_i = 1$ should mean that the optical energy transfer to both $L_{i-1}^{(L)}$ and $L_{i+1}^{(L)}$ is prohibited so that $x_{i-1} = x_{i+1} = 0$ is satisfied. Therefore, the feedback or control mechanism is as follows:

[Control mechanism] If $x_i = 1$ at cycle t , then the control light beams C_{i-1} and C_{i+1} are turned on at cycle $t = t+1$.

In the case of $N = 4$, there are in total 2^4 optical energy transfer patterns from the smaller dot to larger ones. In this case, variables satisfying the constraints do exist, and they are given by $\{x_1, x_2, x_3, x_4\} = \{0, 1, 0, 1\}$ and $\{1, 0, 1, 0\}$, which we call “correct solutions”. Figure 1.6d schematically represent some of the possible states, where the states (7) and (10) respectively correspond to the correct solutions.

We now make a few remarks regarding the NOR problem. One is about potential deadlock, analogous to Dijkstra’s “*dining philosophers problem*”, as already argued by Aono et al. in reference [66]. Starting with an initial state $x_i = 0$ for all i , and assuming a situation where optical energy is transferred to all larger QDs, we observe

photon radiation from all energy levels $L_i^{(L)}$, namely, $x_i = 1$ for all i . Then, based on the feedback mechanism shown above, all control light beams are turned on. If such a feedback mechanism perfectly inhibits the optical energy transfer from the smaller QD to the larger ones at the next step $t + 1$, the variables then become $x_i = 0$ for all i . This leads to all control light beams being turned off at $t + 2$. In this manner, all variables constantly repeat a periodic switching between $x_i = 0$ and $x_i = 1$ in a synchronized manner. Consequently, the system can never reach the correct solutions. However, as indicated in Fig. 1.6c, the probability of optical energy transfer to larger dots is in fact not zero even when all larger QDs are illuminated by control light, as shown in Fig. 1.6c, 4. Also, even for a non-illuminated destination QD, the energy transfer probability may not be exactly unity. Such a stochastic behavior of the optical energy transfer is a key role in solving the NOR problem. This nature is similar to the demonstrations in amoeba-based computing [66] where fluctuations of chaotic oscillatory behavior involving spontaneous symmetry breaking in the amoeboid organism guarantee such a critical property.

The operating dynamics cause one pattern to change to another one in every iteration cycle. Thanks to the stochastic nature, each trial could exhibit a different evolution of the energy transfer patterns. In particular, the transition probability, shown in Fig. 1.6c, affects the behavior of the transitions.

The curves in Fig. 1.7a represent the evolution of the output appearance from QD_{L_i} , namely, the ratio of the incidence when $x_i = 1$ among 1,000 trials evaluated at each cycle. The curves in Fig. 1.7b characterize the ratio of the appearance of the state that corresponds to the correct solutions: $\{0, 1, 0, 1\}$ (state 7) and $\{1, 0, 1, 0\}$ (state 10). When we closely examine the evolutions of x_i in Fig. 1.7a, we can see that the pair x_1 and x_3 exhibit similar behavior, as do the pair x_2 and x_4 . Also, the former pair exhibit larger values, whereas the latter pair exhibit smaller values, and vice versa. This corresponds to the fact that correct solutions are likely to be reached as the iteration cycle increases.

Such a tendency is more clearly represented when we evaluate the time-averages of the characteristics in Fig. 1.7a, b. Figure 1.7c shows the evolutions of the ratio of the incidences when $x_i = 1$, and Fig. 1.7d shows the ratios of State (7) and State (10) averaged over every 5 cycles. We can clearly observe a similar tendency to the one described above. Also, we should emphasize that, thanks to the probabilistic nature of the system, the states of correct solutions appear in an interchangeable manner. This is a clear indication of the fact that the probabilistic nature of the system autonomously seeks the solutions that satisfy the constraints of the NOR problem; the state-dependent probability of energy transfer plays a critical role in this. In other words, it should be emphasized that a non-local correlation is manifested in the evolution of x_i ; for instance, when the system is in State (7), $\{0, 1, 0, 1\}$, the probabilities of energy transfer to QD_{L_1} and QD_{L_3} are equally comparably low (due to state filling), whereas those to QD_{L_2} and QD_{L_4} are equally comparably high, indicating that the probability of the energy transfer to an individual QD_{L_i} has inherent spatial patterns or non-local correlations. At the same time, the energy transfer to each QD_{L_i} is indeed probabilistic; therefore, the energy transfer probability to, for

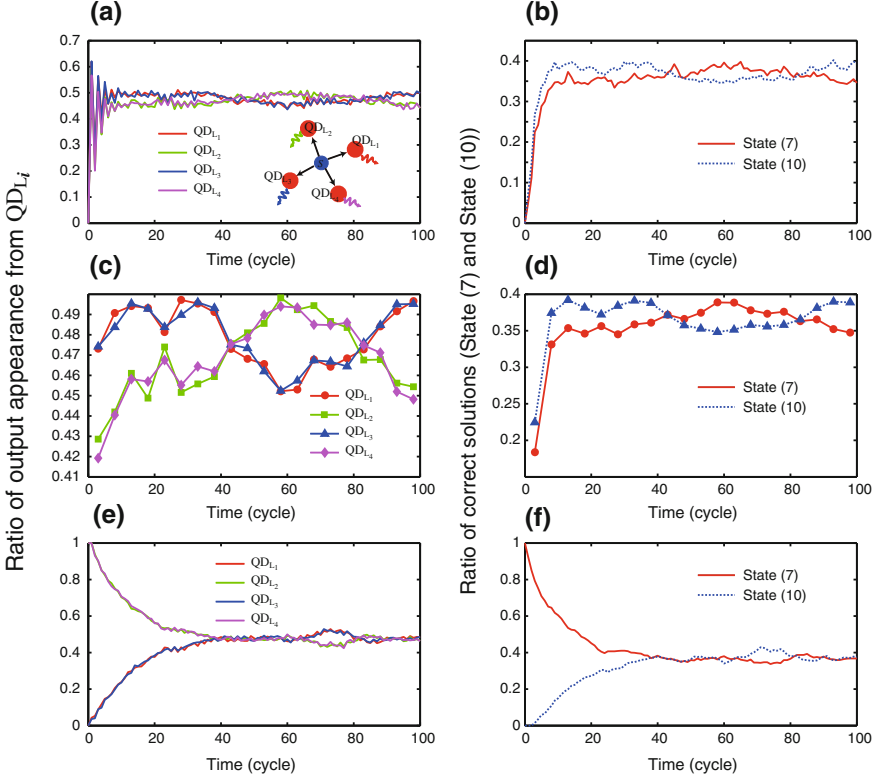


Fig. 1.7 **a** The evolution of the ratio of the output appearance from QD_{L_i} , or $x_i = 1$, and **b** the ratios of the states corresponding to the correct solutions with the initial state of $\{x_1, x_2, x_3, x_4\} = \{0, 0, 0, 0\}$. **c, d** Time-averaged traces of **(a)** and **(b)**, respectively. **e** The evolution of the ratio of the output appearance from QD_{L_i} , or $x_i = 1$, and **f** the ratios of the states corresponding to correct solutions with the initial state $\{x_1, x_2, x_3, x_4\} = \{0, 1, 0, 1\}$

instance, QD_{L1} is not zero even in State (7), and thus, the state could transition from State (7) to State (10), and vice versa. In fact, starting with the initial condition of State (7), the ratio of the output appearance from QD_{L1} and the ratio of the correct solutions evolve as shown in Fig. 1.7e, f, where States (7) and (10) occur equally in the steady state at around 20 time cycles.

We make two final remarks to conclude this section. The first is about the relevance to a satisfiability problem (SAT). In the case of $N = 4$, solving the NOR problem demonstrated above is equivalent to solving the following satisfiability problem instance given in a conjunctive normal form:

$$\begin{aligned}
f(x_1, x_2, x_3, x_4) = & (\neg x_1 \vee \neg x_2) \wedge (\neg x_1 \vee \neg x_4) \wedge (\neg x_2 \vee \neg x_3) \\
& \wedge (\neg x_3 \vee \neg x_4) \wedge (x_1 \vee x_2 \vee x_3) \wedge (x_1 \vee x_2 \vee x_4) \\
& \wedge (x_1 \vee x_3 \vee x_4) \wedge (x_2 \vee x_3 \vee x_4).
\end{aligned} \tag{1.7}$$

Since the maximum number of literals in clauses in (1.7) is three, this is an instance of a so-called 3SAT problem [68]. We have already reported that such a SAT problem could be dealt with by variants of our optical-near-field-mediated systems [69]. SAT is an important nondeterministic polynomial-time complete (NP-complete) problem, indicating that no fast algorithm has been found yet [68]. We consider that nanophotonic principles could potentially provide a new way to solve such computationally demanding problems. In addition, Kim et al. have succeed in applying optical excitation transfer to decision making applications, giving better performance than conventional approaches [70].

The second remark is about the implementation of optical energy transfer for such stochastic computing applications. As mentioned in the introduction, rapid advancements have been made recently in nanomaterials for optical energy transfer [19, 20, 26, 51, 57]. Among various technologies, for example, Akahane et al. successfully demonstrated energy transfer in multi-stacked InAs QDs, where layer-by-layer QD size control has been accomplished [51]. Adequate QD size control also allows optical coupling between optical far-fields and optically-allowed energy levels in a quantum dot mixture, which could help to solve the interfacing issues of the system.

1.3 Nanophotonics for Security

The security aspects of optics have been studied extensively [4], and some of them have been commercialized, such as in optical document security [71]. However, since all of the existing optical security principles and technologies are based on optical far-fields, or propagating light, such as Fourier optics [46], they suffer from associated limitations, such as the difficulty of miniaturizing devices and systems beyond dimensions limited by the diffraction of light [8], leading also to the difficulty in applying them to tamper-resistant hardware in embedded systems etc.

On the other hand, nanophotonics, which utilizes light and matter interactions at scales below the wavelength of light, has recently attracted attention [11]. In addition to the ability to break through the diffraction limit of light, we can also make use of the unique physical processes in nanophotonics, such as optical energy transfer via optical near-field interactions, as discussed in Sect. 1.2. For example, from a security standpoint, the tamper resistance of optical excitation transfer has been demonstrated [72].

At the same time, for tamper-resistant hardware, we can make use of electromagnetic fields in the subwavelength regime, in other words, near-field optics or nano-optics [8]. In particular, technologies allowing shape-engineering of nanostructures,

such as electron beam lithography, are stable and reliable technologies for implementing systems and devices. We have demonstrated a “*hierarchical hologram*” that works in both optical far-fields and near-fields, the former being associated with conventional holographic images, and the latter being associated with the optical intensity distribution originating from a nanometric structure embedded in the hologram, which is accessible only via optical near-fields [22, 73, 74]. In other words, information hiding can be realized by using optical near-fields and nanofabrication technologies. Also, authentication functions can be implemented by using two shape-engineered nanostructures and their associated optical near-fields [21, 75]. In this system, the two nanostructures respectively work as a *lock* and *key*, where authenticity is guaranteed by the nanoscale-precision shapes of the structures.

As described above, the physical principles of nano-optics will contribute to novel security means. However, from a security perspective, more-solid theoretical foundations and performance evaluations are necessary. In this section, we present a fundamental theory of nano-optics based on a rigorous treatment and evaluate its associated performance. We then characterize particular examples of nano-optical security means based on this theoretical foundation. These investigations will lead to enriched tamper-resistant hardware utilizing nano-optical processes, such as physical unclonable functions (PUFs) or security technologies in embedded systems in general.

1.3.1 Theoretical Foundation

Optical near-fields are the localized, non-propagating components of electromagnetic fields in the vicinity of materials [8]. We need to locate certain kinds of *reader* to induce interactions between the material under study and the reader. In order to characterize the structure of the system, we denote the entities of the system as follows. Let the material under study, or the device, be denoted by D , and the reader by R . The output signal is written as $v = g(D, R)$.

One of the characteristic consequences of nano-optical systems is that the output signal depends sensitively on both D and R , which is represented by the function $g(D, R)$. Such physically inherent properties of nano-optics are well-matched with the architecture of tamper-resistant hardware. In order to theoretically represent the fundamental characters, we describe the system as follows. The device D is represented by a point dipole located a distance X away from the origin, and the reader R is located a distance Z away from the origin, as shown in Fig. 1.8a. The R -dependence of the output signal is regarded as being equivalent to the Z -dependence.

Here, we employ the angular spectrum representation of electromagnetic fields, in which the electromagnetic fields are represented as a superposition of evanescent waves with different decay lengths and corresponding spatial frequencies [76–78]. As well as giving a rigorous analytical treatment of near-field components in the subwavelength regime, this picture can explicitly include the D - and Z -dependences as follows.

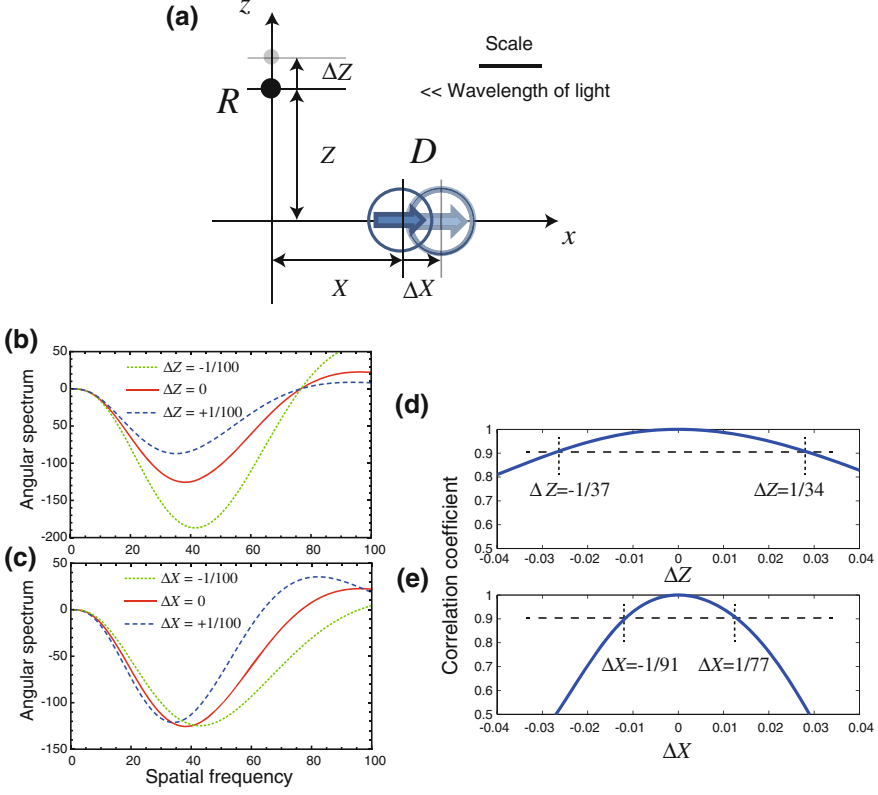


Fig. 1.8 Fundamental system model for nano-optical security. **a** A point dipole (D) and an evaluation point (Z) represent the device under study (D) and the reader (R), respectively. **b, c** The output signal is evaluated by the angular spectrum, which is the near-field component of the electromagnetic field in the subwavelength regime. Differences in Z and X are respectively shown in **(b)** and **(c)**. **d, e** Correlation coefficient of the output signal as a function of minute differences in Z and X . A tiny difference strongly affects the output signal, which is a manifestation of the ability of nano-optics for tamper-resistant hardware, offering functions like anticounterfeiting, authentication, etc.

Suppose that there is an electric dipole, $\mathbf{D} = d(\cos \varphi, 0)$, on the xz plane oscillating at frequency K , as shown in Fig. 1.8a. The velocity of light is taken as unity. Now, consider the electric field of radiation observed at a position displaced from the dipole by $\mathbf{R} = (r_{\parallel} \cos \phi, Z)$. The angular spectrum representation of the z -component of the optical near-field is given by

$$E_z(\mathbf{R}) = \left(\frac{iK^3}{4\pi\epsilon_0} \right) \int_1^\infty ds_{\parallel} \frac{s_{\parallel}}{s_z} f_z(s_{\parallel}, \mathbf{D}, \mathbf{R}), \quad (1.8)$$

where

$$f_z(s_{||}, \mathbf{D}, \mathbf{R}) = ds_{||} \sqrt{s_{||}^2 - 1} \cos(\varphi - \phi) J_1(Kr_{||}s_{||}) \exp\left(-KZ\sqrt{s_{||}^2 - 1}\right). \quad (1.9)$$

Here, $s_{||}$ is the spatial frequency of an evanescent wave propagating parallel to the x axis, and $J_n(x)$ represents Bessel functions of the first kind. The term $f_z(s_{||}, \mathbf{D}, \mathbf{R})$ is called the angular spectrum of the electric field. We consider that $f_z(s_{||}, \mathbf{D}, \mathbf{R})$ is equivalent to the signal $v = g(D, R)$ characterized in the system model. In the case of the system model shown in Fig. 1.8a, the parameters are given by $\varphi = 0$, $r_{||} = X$, and $\phi = \pi$. Note that X and Z can be effectively considered to be given in units of wavelength.

The solid curve in Fig. 1.8b shows the angular spectrum when $X = 1/20$ and $Z = 1/20$. This corresponds to an *authentic* device D and an *authentic* reader R . Differences of the reader R are equivalent to differences of Z ; for instance, when Z is shifted by distance $\Delta Z = -1/100$ the angular spectrum is given by the dotted curve in Fig. 1.8b. Similarly, when $\Delta Z = 1/100$, the angular spectrum is given by the dashed curve in Fig. 1.8b. As shown by the changes of the curve in Fig. 1.8b, the slight difference with respect to Z results in a different output signal from the system. In order to quantitatively evaluate the Z -dependence, the correlation coefficient of the angular spectrum is calculated as a function of ΔZ as summarized in Fig. 1.8d. If we determine that an authentic signal should yield a correlation coefficient larger than 0.9, ΔZ should be between $-1/37$ and $1/34$, which would be an extremely small absolute value in real dimensions. This indicates that nano-optics provides an evident reader-dependence. Similarly, by considering the position of the dipole as the identity of the device, a different position of the dipole provides a different angular spectrum. The solid, dotted, and dashed curves in Fig. 1.8c respectively indicate the angular spectra when ΔX is given by 0, $-1/100$, and $+1/100$. The correlation coefficient is evaluated as shown in Fig. 1.8e; it is larger than 0.9 when ΔX is between $-1/77$ and $1/91$, indicating that the output signal is sensitive to subtle differences of the device D .

1.3.2 Hierarchical Hologram for Information Hiding and its Theoretical Fundamentals

Holography, which generates natural three-dimensional images, is one of the most common anti-counterfeiting techniques [71]. In a volume hologram, the surface is ingeniously formed into microscopic periodic structures that diffract incident light in specific directions. Generally, these microscopic structures are recognized as being difficult to duplicate; therefore, holograms have been widely used in the anti-counterfeiting of bank notes, credit cards, etc. However, conventional anti-counterfeiting methods based on the physical appearance of holograms are nowadays not completely secure [79]. Nano-optical solutions would provide higher

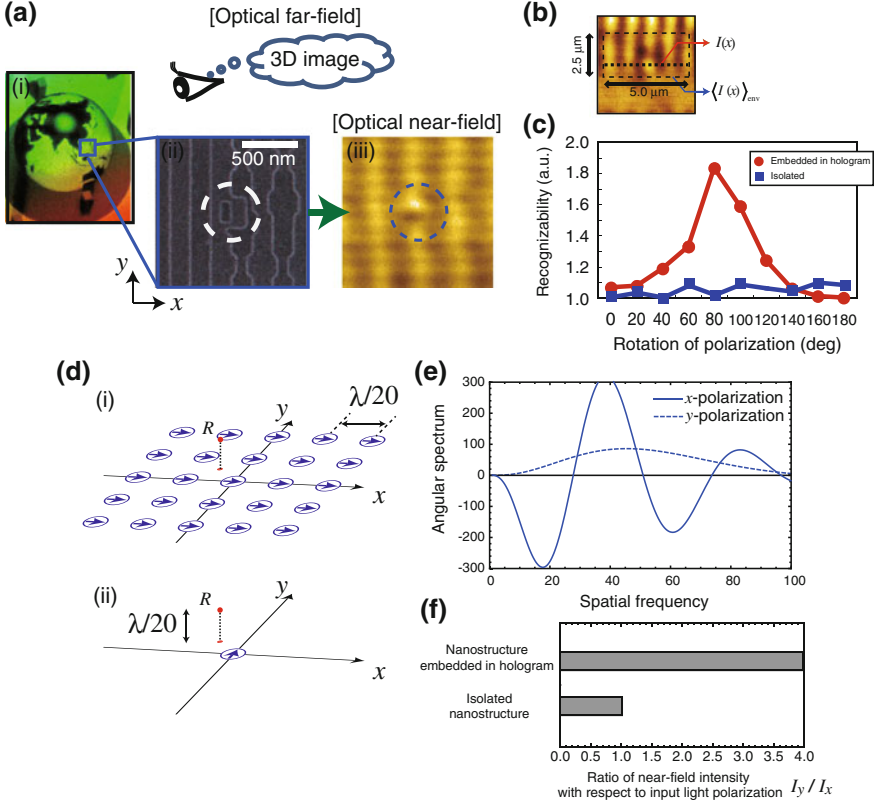


Fig. 1.9 Hierarchical hologram. Experimental demonstrations and theoretical foundations. **a** Hierarchical hologram. **b, c** Polarization dependencies in the near-field retrieval from the nanostructure embedded in the hologram. **d, e, f** Theoretical reasoning of the polarization dependencies of nanostructures embedded in holograms. **d, e** x -polarized light induces an array of dipoles, which results in weaker localization in its near-fields ((**d, i**) and solid curve in (**e**)), whereas y -polarized light induces dipoles only at the nanostructures embedded in the hologram, which results in high localization in its near-fields ((**d, ii**) and dashed curve in (**e**)). **f** These results explain the evident polarization dependencies

anti-counterfeiting capability and could potentially enable other applications, such as artifact-metric systems [80].

A *hierarchical hologram* works in both optical far-fields and near-fields, the former being associated with conventional holographic images (Fig. 1.9a, i), and the latter being associated with the optical intensity distribution originating from a nanometric structure (Fig. 1.9a, ii) that is accessible only via optical near-fields (Fig. 1.9a, iii). In principle, a structural change occurring at the subwavelength scale does not affect the optical response function, which is dominated by propagating light. Therefore, the visual aspect of the hologram is not affected by such a small structural change on the surface. Additional data can thus be written by engineering

structural changes in the subwavelength regime so that they are only accessible via optical near-field interactions, without having any influence on the optical response obtained via the conventional far-field light. As indicated in Fig. 1.9a, i, we can observe a three-dimensional image of the earth reconstructed from the device. More specifically, the device was based on the design of *Virtuagram*®, developed by Dai Nippon Printing Co., Ltd., Japan, which is a high-definition computer-generated hologram composed of binary-level one-dimensional modulated gratings, as shown in the scanning electron microscope (SEM) image in Fig. 1.9a, ii. Within the device, we slightly modified the shape of the original structure of the hologram so that the nanostructural change was accessible only via optical near-field interactions. As shown in Fig. 1.9a, ii, square- or rectangle-shaped structures, whose associated optical near-fields correspond to the additional or hidden information, were embedded in the original hologram structures. The unit size of the nanostructures ranged from 40 to 160 nm.

The original hologram structure is basically composed of one-dimensional gratings; that is, the structure is topologically connected along the vertical direction. The embedded nanostructure for the hidden information destroys such a connected topology of the original gratings.

From a security standpoint, we should mention two points. One is that counterfeiting such an intricate nanostructure would be technologically very difficult, if not impossible, since realizing the minimum feature size—40 nm in the device shown in Fig. 1.9a [22]—would require the attackers to have high-quality nanofabrication facilities. The other is that such a *topologically disconnected* structure exhibits strong polarization dependence. The input light induces oscillating surface charge distributions due to the coupling between the light and electrons in the metal. Note that the original 1D grid structures span along the vertical direction. The *y*-polarized input light induces surface charges along the vertical grids. Since the grid structure continuously exists along the *y*-direction, there is no chance for the charges to be concentrated. However, in the area of the embedded square-shaped nanostructure, we can find structural discontinuity in the grid; this results in higher charge concentrations at the edges of the embedded nanostructure. On the other hand, the *x*-polarized input light sees structural discontinuity along the horizontal direction due to the vertical grid structures, as well as in the areas of the embedded nanostructures. It turns out that charge concentration occurs not only in the edges of the embedded nanostructures but also at other horizontal edges of the environmental grid structures. When a square-shaped nanostructure is *isolated* in a uniform plane, both *x*- and *y*-polarized input light have equal effects on the nanostructures. The nanostructures embedded in holograms could exploit these polarization dependences.

In the experimental demonstration, near-field intensity distributions were detected using a near-field optical microscope operated in an illumination-collection mode with an optical fiber tip having a radius of curvature of 5 nm. The observation distance between the tip of the probe and the sample device was set at less than 50 nm. The light source used was a laser diode (LD) with an operating wavelength of 785 nm, and scattered light was detected by a photomultiplier tube (PMT). We examined near-field images in the vicinity of nanostructures that were embedded in the hologram and

nanostructures that were not embedded in the hologram using a linearly polarized radiation source with its polarization rotated from 0° to 180° at 20° intervals. In the case of nanostructures embedded in the hologram, clear polarization dependence was observed. To quantitatively evaluate the polarization dependence, we adopted a figure-of-merit, what we call *recognizability*, for the observed near-field images, which represents the difference of the near-field intensity compared with that of neighboring areas. More specifically, let the horizontal intensity profile along the dashed line in Fig. 1.9b, which crosses the area of the nanostructure, be denoted by $I(x)$, where x represents the horizontal position. Also, let the average intensity along the vertical direction at the horizontal position x within a range of $2.5\ \mu\text{m}$ be denoted by $\langle I(x) \rangle_{\text{env}}$, which indicates the environmental signal distribution. When a higher intensity is obtained selectively from the area of the nanostructure, the difference between $I(x)$ and $\langle I(x) \rangle_{\text{env}}$ should be large. On the other hand, if the intensity distribution is uniform along the vertical direction, the difference between $I(x)$ and $\langle I(x) \rangle_{\text{env}}$ should be small. Thus, the difference between $I(x)$ and $\langle I(x) \rangle_{\text{env}}$ indicates the *recognizability* of the nanostructures. With respect to the polarization angle θ , we evaluate the *recognizability* $R(\theta)$ as $R(\theta) = \sum_x |I(x) - \langle I(x) \rangle_{\text{env}}|$. The square and circular marks in Fig. 1.9c respectively show $R(\theta)$ based on the near-field images of isolated nanostructures and those embedded in the hologram. Clear polarization dependency is observed in the case of the nanostructures embedded in the hologram.

Here, we theoretically deal with the above properties of a hierarchical hologram using the theoretical elements presented in Sect. 1.3.1. As mentioned earlier, x -polarized input light sees structural discontinuity along the horizontal direction due to the vertical grid structures, as well as in the areas of the embedded nanostructures. We represent such a situation by a 5×5 array of dipoles arranged in the xy plane, as shown in Fig. 1.9d, and assume that the dipole located at the center corresponds to the nanostructure implemented for the information hidden within the hologram. We consider the electromagnetic field in the vicinity of the embedded nanostructure at the position R in Fig. 1.9d, i.

The angular spectrum is calculated by summing up all contributions from the 5×5 dipoles at the point R , as shown by the solid curve in Fig. 1.9e, which oscillates as a function of spatial frequency, indicating that the field is not strongly localized at point R . On the other hand, when the y -polarized input light is irradiated, the charge concentration occurs only at the embedded nanostructure, which is represented by Fig. 1.9d, ii. The corresponding angular spectrum at point R is given by the dashed curve in Fig. 1.9e. It exhibits a peak value at a certain spatial frequency, meaning that the higher intensity electric field is localized at point R . Such a difference is one theoretically predicted behavior that is observed experimentally. By calculating the integrals of the angular spectrum with respect to x - and y -polarized input light, which respectively represent the near-field intensities given by I_x and I_y , the ratio of the two, I_y/I_x , results in a value of about 4. In the case of isolated nanostructures, since both x - and y -polarized light components induce the same responses, and the corresponding ratio is unity, as summarized in Fig. 1.9f, these theoretical investigations are consistent with the experimental observations shown in Fig. 1.9c.

1.3.3 Shape-Engineered Nanostructures for Authentication Functions

In this section, we demonstrate that two metal nanostructures, called *Shape D* and *Shape R*, can be designed to exhibit far-field radiation only when their shapes are appropriately configured and when they are closely stacked [21, 75]. Such functionality is useful in ensuring authentication or certification, where a system should work only when the two nanostructures match, just like a *lock* and *key*. We explain the operating principle by observing the induced electric currents and their associated optical near-fields based on the theoretical elements presented in Sect. 1.3.1.

We have previously proposed a theoretical scheme that is useful for examining the relation between the shapes of nanostructures and the resulting light polarization in their optical near-field and far-field [81]. In that study, the geometry of a given nanostructure can be understood in terms of two factors, “individual element” and “layout”, where the former represents the shapes of individual elements, and the latter their spatial arrangement. There are two important physical aspects in analyzing their corresponding optical responses. One is that input light induces electric currents within individual elements of the metal nanostructure. The other is optical near-fields between those individual elements. We can understand those two processes in a unified manner as vectorial elements in the system [81].

Shape D and Shape R were designed as rectangular units aligned on an xy -plane at constant intervals horizontally (along the x -axis) and vertically (along the y -axis), as respectively shown in Fig. 1.10a, b. When we irradiate Shape D with x -polarized light, surface charges are concentrated at the horizontal edges of each of the rectangular units. The relative phase difference of the oscillating charges between the horizontal edges is π , which is schematically represented by $+$ and $-$ marks in Fig. 1.10a. Now, consider the y -component of the far-field radiation from Shape D, which is associated with the charge distributions induced in the rectangle. When we draw arrows from the $+$ marks to the $-$ marks along the y -axis, we find that adjacent arrows are always directed oppositely, indicating that the y -component of the far-field radiation is externally small. In other words, Shape D behaves as a quadrupole regarding the y -component of the far-field radiation. It should also be noted that near-field components exist in the vicinity of the units in Shape D. With this fact in mind, we put the other metal nanostructure, Shape R, on top of Shape D. Through the optical near-fields in the vicinity of Shape D, surface charges are induced on Shape R. What should be noted here is that the arrows connecting the $+$ and $-$ marks along the y -axis are now aligned in the same direction, and so the y -component of the far-field radiation appears; that is, the stacked structure of Shape D and Shape R behaves as a dipole (Fig. 1.10c). Also, Shape D and Shape R need to be closely located to invoke such effects since the optical near-field interactions between Shape D and Shape R are critical. In other words, far-field radiation appears only when Shape D and Shape R are correctly stacked.

We fabricated structures consisting of (i) Shape D only, (ii) Shape R only, and (iii) Shape D and Shape R stacked. Although the stacked structure should ideally

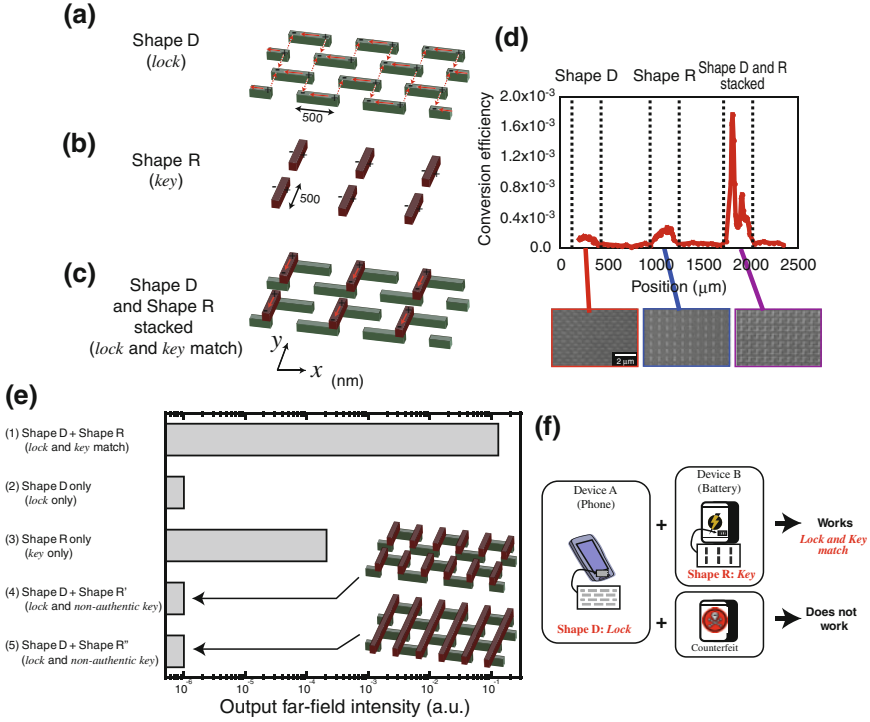


Fig. 1.10 Authentication, or *lock* and *key*, based on nano-optics. **a** Shape D, **b** Shape R, and **c** stacked structure of Shapes D and R. **d** Experimental demonstration of the lock and key matching, where a strong output signal appears only when Shape R matches Shape D. **e** Lower output signals when *non-authentic keys* are stacked on top of the *lock*. **f** An application of authentication based on nano-optics. Shape D on a mobile phone and Shape R on a certified battery

be formed by combining the individual single layer structures, in the experiment, the stacked structure was integrated in a single sample as a solid two-layer structure to avoid the experimental difficulty in precisely aligning the individual structures mechanically. The fabrication process was detailed in [21]. The lower side in Fig. 1.10d also shows SEM images of fabricated samples of (i), (ii), and (iii). The performance was evaluated in terms of the polarization conversion efficiency by radiating x -polarized light on each of the areas (i), (ii), and (iii) and measuring the intensity of the y -component in the transmitted light. The light source was a laser diode with an operating wavelength of 690 nm. Two sets of polarizers (extinction ratio 10^{-6}) were used to extract the x -component for the input light and to extract the y -component in the transmitted light. The intensity was measured by a lock-in controlled photodiode. Figure 1.10d shows the polarization conversion efficiency as a function of the position on the sample, where it exhibited a larger value specifically in the areas where the stacked structure of Shapes D and R was located, which agrees well with the theoretically predicted results.

From the theoretical standpoint presented in Sect. 1.3.1, what is important to obtain y-polarized output light is to locate an appropriately-designed Shape R on top of Shape D with high alignment accuracy so that coherently phased dipoles are induced in Shape R. As the theoretical results in Sect. 1.3.1 suggest, high-precision control and alignment is essential to induce the output light.

In Fig. 1.10e, we consider the output signals when we place differently-shaped structures on top of Shape D, instead of Shape R. That is, we intentionally put *non-authentic keys* on top of the lock. The far-field output light is evaluated by finite-difference time-domain (FDTD) electromagnetic simulations. The designs of Shape D and Shape R consist of arrays of gold rectangular units; each unit has a length of 500 nm, and a width and a height of 100 nm. As the material, we assumed the Drude model of gold with a refractive index of 0.16 and an extinction ratio of 3.8 at a wavelength of 688 nm. With Shape R' and Shape R'', which are respectively represented in the insets of Fig. 1.10e, as well as with the *lock-only* and *key-only* shapes, the output signals do not appear, as shown from the fourth to the fifth row in Fig. 1.10e, since the condition necessary for far-field radiation is not satisfied with those shapes; namely, the correct *key* is necessary to unlock the *lock*.

Such functionality is useful, as mentioned in the beginning of this section, in ensuring hardware authentication, where a system should work only when the two nanostructures match. This would provide novel applications in the authentication of ubiquitous devices. For instance, the explosion of non-certified batteries is a serious issue in mobile devices [82]; the nano-optical lock-and-key principles and technologies described here could mitigate this problem by locating Shape D on the mobile phone and a corresponding Shape R on a certified battery, as schematically shown in Fig. 1.10f.

1.4 Stochastic Modeling of Near-Field Processes for Intelligent Material Formation

Precision control of the geometrical features of materials on the nanometer scale, such as their sizes and positions, are important factors in obtaining the intended functionalities of nanophotonic devices and systems in which multiple nanostructures interact via optical near-fields [11], and also for plasmonic devices [83]. For example, the sizes of QDs should be well-controlled to ensure that the quantized energy levels between adjacent QDs are resonant, to facilitate efficient optical near-field interactions [24]. Arrays of nanoparticles are important in various applications, such as nanophotonic devices [11], optical far-field to near-field converters, plasmonic light transmission lines [84], etc.

To satisfy such requirements, light-assisted, self-organized nanostructure fabrication principles and techniques have been developed [33, 34]. One example is the sol-gel synthesis of ZnO quantum dots (QDs) using photo-induced desorption, which yields QDs with reduced variations in diameter [33]. Another example of

light-assisted nanostructure fabrication is metal sputtering with light irradiation, which produces self-organized, size- and position-controlled metal nanoparticle chains [34]. In addition to the superior ability in regulating the geometries of nanostructures, these light-assisted, self-organized fabrication techniques have relatively simple experimental setups and have superior production throughput compared with, for instance, scanning-based methods, such as those based on scanning architectures [85, 86].

The physical mechanisms behind light-assisted nanostructure formation have been attributed to material desorption [33, 87, 88] or plasmon resonance between light and matter. However, stochastic physical processes are also present, as observed in the experimental data discussed below. Also, we consider that a stochastic approach is indispensable for taking account of the emergence of ordered structures and for the purpose of obtaining intended structures; in other words, for achieving “*nanointelligence*” in material production.

In light of this background, we approach light-assisted nanofabrication from a stochastic standpoint. Taking account of light-assisted processes, we build stochastic models that reproduce tendencies consistent with experimental observations. Through such considerations, we obtain critical insights into order formation on the nanometer scale, which will contribute to the design of nanophotonic devices and systems.

1.4.1 Light-Assisted Size-Regulation of Nanoparticles

First, we characterize the light-assisted, self-organized ZnO quantum dot formation, which was experimentally demonstrated in reference [33], with a stochastic approach. We first briefly review the experimental observations. In making ZnO QDs, synthetic methods using liquid solutions are advantageous because of their need for simple facilities and their high productivity [89] compared with other techniques [90, 91]. In conventional sol-gel methods [89], however, the size of the QDs varies by as much as 25 %. Liu et al. demonstrated a light-assisted sol-gel method that reduced the QD diameter variations [33]. When light with a photon energy higher than the bandgap energy is radiated during the ZnO QD formation process, electron-hole pairs could trigger an oxidation-reduction reaction in the QDs, causing the ZnO atoms depositing on the QD surface to be desorbed. In addition, such desorption is induced with a high probability when the formed QDs reach a particular diameter. This light-dependent QD size regulation has also been reported in other material systems, such as CdSe [87] and Si [88].

The insets in Fig. 1.11a, b respectively show transmission electron microscope (TEM) images of fabricated ZnO QDs without and with continuous-wave (CW) light illumination at a wavelength of 325 nm with a power density of 8 mW cm^{-3} [33]. Figures 1.11a, b respectively summarize the incidence rate of nanoparticles as a function of their diameter, whose variations decreased from 23 to 18 % with light irradiation. In particular, note that the diameter distributions are different between

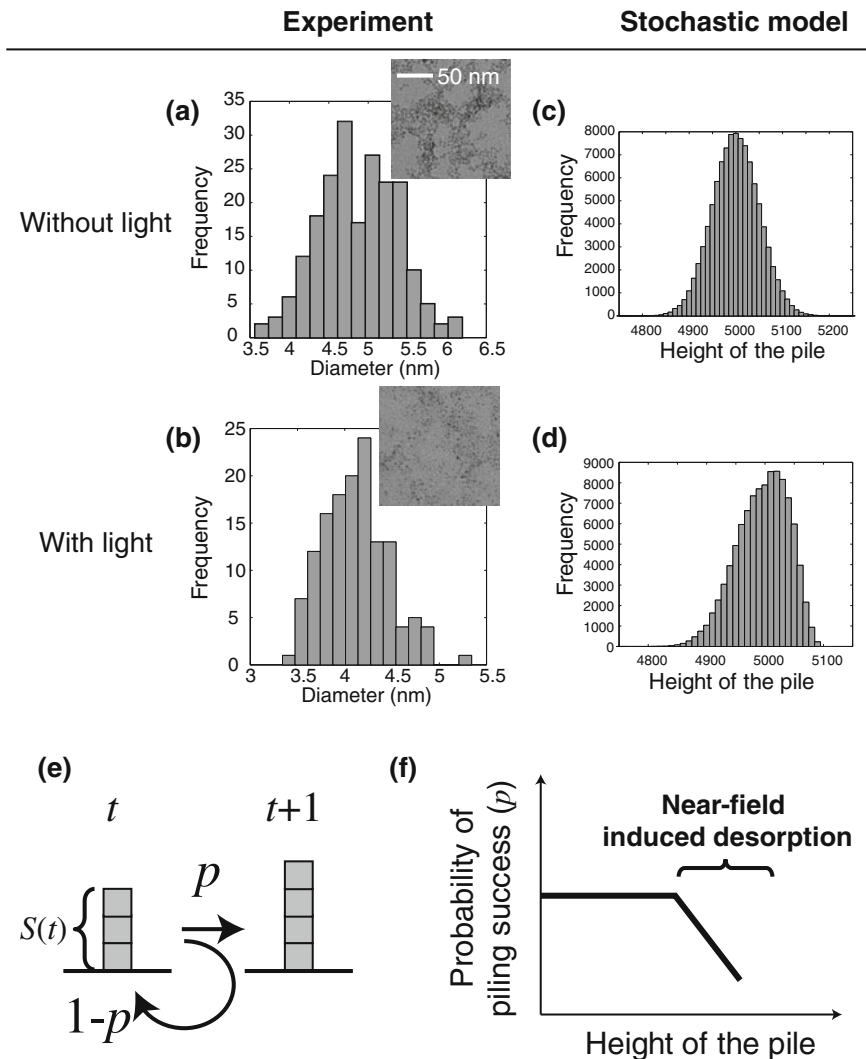


Fig. 1.11 Incidence patterns of the diameters of fabricated ZnO quantum dots (QDs) formed by a sol-gel method **a** without light irradiation and **b** with light irradiation. Insets in **(a)** and **(b)** are transmission electron microscope images of QDs without and with light irradiation, respectively. **c, d** Incidence patterns of the size distribution generated with the proposed stochastic model. The patterns are consistent with the experimental observations in **(a)** and **(b)**. **e** A stochastic model of light-assisted nanoparticle formation. The growth of the QD is characterized with a one-dimensional pile-up model. The success of the piling depends on probability p . **f** The effect of light irradiation is modeled by a decrease in the probability p beyond a certain pile height, which corresponds to the diameter of the nanoparticle in the experiment

these two cases. Without light illumination (Fig. 1.11a), it exhibits behavior similar to a normal distribution. In contrast, with light irradiation, the distribution is skewed; in particular, the incidences at larger diameters decreased (Fig. 1.11b). We investigate this different behavior by means of stochastic modeling.

First, in the absence of light illumination, we represent the formation process with a statistical pile-up model, as schematically shown in Fig. 1.11e. An elemental material that constitutes a nanoparticle is represented by a square-shaped block. Such blocks are grown, or stacked one on another, with a piling success probability p ; accordingly, the piling fails with a probability of $1 - p$. In other words, if we let the height of the pile at step t be $s(t)$, the piling probability is given by

$$\begin{cases} P[s(t+1) = s(t) + 1 | s(t)] = p \\ P[s(t+1) = s(t) | s(t)] = 1 - p. \end{cases} \quad (1.10)$$

Since this is equivalent to a random walk with drift, after repeating this process with an initial condition $s(0) = 0$, the resultant heights of the piles exhibit a normal distribution, as shown in Fig. 1.11c. Specifically, the statistics shown in Fig. 1.11c were obtained by repeating 10,000 steps for 100,000 different trials.

On the other hand, we model the effect of light irradiation in the formation process in the stochastic model as follows. As described above, since the material desorption is likely to be induced at a particular nanoparticle diameter, we consider that the piling success rate p is a function of the diameter, namely the height of the pile. For simplicity, we consider that p , which represents the deposition success probability, decreases linearly beyond a certain total pile height, as schematically shown in Fig. 1.11f. In other words, the material desorption is more likely to be induced beyond a certain pile size due to the resonant effect mentioned above. That is, the probability p in (1.10) is replaced with the following size-dependent probability:

$$p(s(t)) = \begin{cases} c & s(t) \leq R \\ c - \alpha s(t) & s(t) > R \end{cases}, \quad (1.11)$$

where c and α are constants. With such a stochastic model, the resultant incidence distributions of the piles are skewed or reduced at larger sizes. In the calculated results shown in Fig. 1.11d, we assume $c = 1/2$ and $\alpha = 1/250$. The numerical results obtained through the statistical modeling are consistent with the experimental observations.

1.4.2 Light-Assisted Nanoparticle Array Formation

Yatsui et al. demonstrated self-organized formation of an ultralong array of nanoparticles based on near-field optical desorption (Fig. 1.12a, b) [34]. We first briefly describe the experimental observations. With conventional radio-frequency (RF) sputtering, aluminum was deposited on a glass substrate. A 100nm-wide and

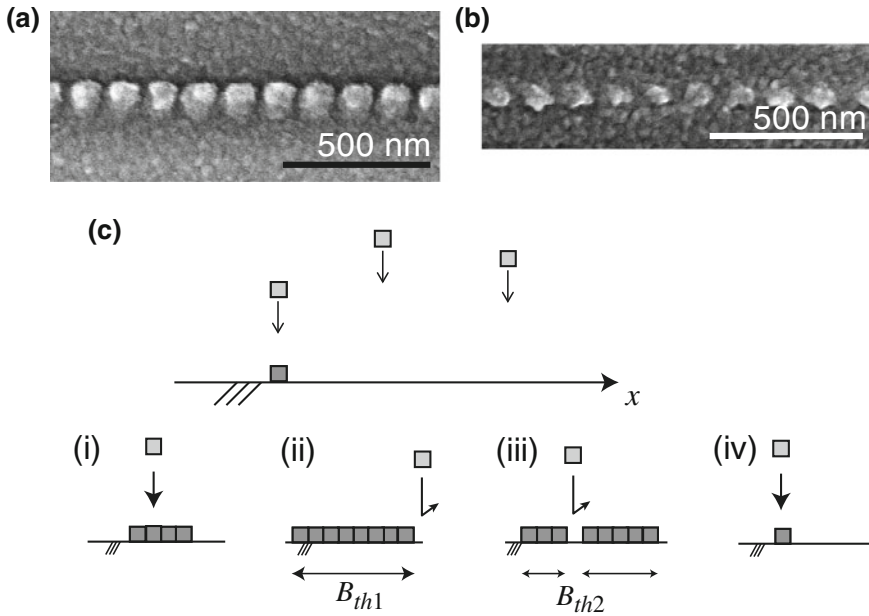


Fig. 1.12 An array of uniform-diameter, uniform-separation Al nanoparticles is self-organized along a groove, with **a** 2.33 eV light irradiation and **b** 2.62 eV light irradiation. **c** A stochastic model of the nanoparticle array formation. One-dimensional array in which an elemental block could be deposited at position x . (i)–(iv) Rules for successful deposition at a randomly chosen position x . (i) When the position belongs to one of the clusters, the cluster is maintained. (ii) Deposition is inhibited next to a cluster whose size is larger than B_{th1} . (iii) Deposition is inhibited at a position where the block sees clusters at both the left- and right-hand sides and when the total size of both clusters is larger than B_{th2} . (iv) In other cases, deposition at the position succeeds

30-nm-deep groove was formed in the substrate. Also, the substrate was illuminated with light linearly polarized perpendicularly to the direction of the groove during the RF sputtering. Thanks to the well-defined edge of the groove, a strong optical near-field was generated in its vicinity.

A metallic nanoparticle has strong optical absorption because of plasmon resonance that depends strongly on the particle size [92–94]. This can induce desorption of a deposited metallic material when it reaches the resonant diameter [95, 96]. It turns out that, as the deposition of the metallic material proceeds, the growth is governed by a tradeoff between deposition and desorption, which determines the particle diameter, depending on the photon energy of the incident light. Consequently, an array of metallic nanoparticles is aligned along the groove. While radiating continuous-wave (CW) light with a photon energy of 2.33 eV (wavelength: 532 nm) during the deposition of aluminum, 99.6-nm-diameter, 27.9-nm-separation nanoparticles were formed in a region as long as 100 μm (Fig. 1.12a).

As described above, the origin of the size regulation of the nanoparticles was attributed to the resonance between the nanoparticles and the illuminated light,

similarly to the case discussed in Sect. 1.4.1. At the same time, we consider that although this physical mechanism indeed plays a crucial role, it is not enough to explain the formation of the uniformly formed array structure. To explain such an observation, we need to extend the stochastic model described in Sect. 1.4.1 as follows.

In the modeling, we assume a one-dimensional horizontal system that mimics the groove on the substrate; it consists of an array of N pixels identified by an index i ranging from 1 to N . An elemental material to be deposited onto the system, experimentally by the RF sputtering described above, is schematically represented by a square-shaped block (Fig. 1.12c). The initial condition is a flat structure without any blocks.

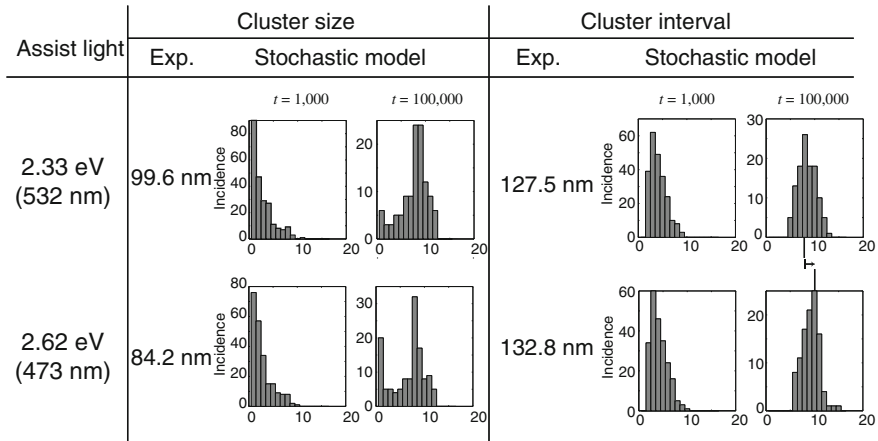
At every iteration cycle, the position at which a block arrives, denoted by x , is randomly chosen. We determine the success of the deposition at x by the following rules. We denote the occupation by a block at position x of the groove by $S(x)$; $S(x) = 1$ when a block occupies a position x , and $S(x) = 0$ when there is no block at position x . Also, we use the term “cluster” to mean multiple blocks consecutively located along the groove. We also call a single, isolated block in the system a “cluster”.

1. When the randomly chosen position x belongs to one of the cluster(s), namely, $S(x) = 1$, we maintain $S(x) = 1$ (Fig. 1.12c, i).
2. Even if $S(x) = 0$, when the chosen position x belongs to a “neighbor” of a cluster with a size greater than a particular number B_{th1} , the deposition is inhibited. That is, we maintain $S(x) = 0$ (Deposition is inhibited.) (Fig. 1.12c, ii).
3. Even if $S(x) = 0$, when the chosen position x has blocks at both its left and right sides and the total number of connected blocks is greater than B_{th2} , the deposition is inhibited. That is, we maintain $S(x) = 0$ (Fig. 1.12c, iii).
4. In other cases, the deposition at position x succeeds; namely, $S(x) = 1$ (Fig. 1.12c, iv).

The rules (ii) and (iii) correspond to the physical effect of the resonance between the material and the light illumination that facilitates desorption of the particle. The optical near-field intensity in the vicinity of a nanostructure follows a Yukawa function (1.6). Therefore, the optical near-fields promote material desorption, or in effect, inhibit material deposition, beyond a certain size of nanoparticles, which is characterized as rule (ii) above. Also, even when a single cluster size is small, meaning that the corresponding near-fields are small, when several such clusters are located in close proximity, a material desorption effect should be induced overall. Such an effect is represented as rule (iii) above. One remark here is that we do not pile more than two blocks at a single position x ; that is to say, $S(x)$ takes binary values only, since our concern is how the clusters are formed in the 1D system.

Figure 1.13a shows the results of a numerical demonstration assuming a 1D array with $N = 1,000$. As statistical values in the simulations, we evaluated the incidence of the cluster size and the center-to-center interval between two neighboring clusters. Figure 1.13a summarizes the evolution of these two values at $t = 1,000$ and $t = 100,000$. In the numerical calculations, for the threshold values in rules (ii) and (iii), we assumed $B_{th1} = 8$ and $B_{th2} = 12$, respectively. We clearly observed that the

(a)



(b)

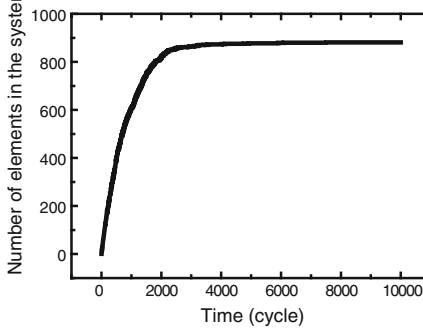


Fig. 1.13 **a** Evolution of the cluster size and the cluster interval based on a stochastic model. Both the size and the interval converge to incidence patterns that exhibit maxima at a particular value, which reproduced the experimentally observed size- and separation-controlled formation of a nanoparticle array. The interval of the nanoparticles is greater with higher photon energy. By modifying rule (ii) of the stochastic model, the cluster interval increases, which is consistent with the experimental observations. **b** Evolution of the number of elements in the stochastic model. After cycle $t = 3,000$, the number of elements is stable, meaning that the system is getting into a steady state in a self-organized manner

size and the interval converged to representative values, which is consistent with the experimental observations shown in Fig. 1.12a. Furthermore, we evaluate the total number of elemental blocks contained in the system as a function of elapsed time in the stochastic simulation. As shown in Fig. 1.13b it converges to a constant value beyond around 3000 iteration cycles, which is another indication that a self-organized process emerges based on optical near-field processes. Since the present modeling includes some parameters, this does not strictly exhibit so-called self-organized criticality [30]. However, we consider that the convergence to a uniformly

sized, uniformly separated 1D pattern is indeed a kind of self-organized critical phenomenon.

Moreover, as reported in reference [34], a similar experiment was conducted with a higher photon energy of 2.62 eV (473 nm) and an optical power of 100 mW, which resulted in the formation of 84.2 nm-diameter, 48.6 nm-separation nanoparticles (Fig. 1.12b). As summarized in the experimental results indicated in Fig. 1.13a, the diameter is slightly reduced and the nanoparticle distance is enlarged compared with the previous case of lower photon energy (2.33 eV (532 nm)). The reduced diameter of the nanoparticles is attributed to the fact that the higher photon energy leads to desorption at smaller diameters [33, 92]. The larger separation between adjacent nanoparticles is, however, not obviously explained.

We presume that a stronger light–matter resonance is induced at a higher photon energy, which more strongly induces material desorption, or inhibits the deposition of materials, in the neighboring clusters. We can take account of this effect by modifying the stochastic model described above. Instead of blocking the deposition at the neighboring positions by rule (ii), we consider that distant neighbors are also inhibited:

(ii') Even if $S(x) = 0$, when x sees a cluster with a size greater than a particular number B_{th1} , within an area (a) between $x - 3$ and $x - 1$ or (b) between $x + 1$ and $x + 3$, the deposition is inhibited. That is, we maintain $S(x) = 0$.

While preserving B_{th1} and B_{th2} values with the previous example, the cluster size statistics evolve as shown in Fig. 1.13a. At the iteration cycles $t = 1,000$ and 100,000, the incidences of single-sized clusters are large. This is due to the strict inhibition rule (ii') above, which reduces the chance of clusters growing. Treating such a single-sized cluster as an artifact, or a virtually ignorable element, in the system, we evaluate the cluster-to-cluster interval except for single-sized clusters. The cluster interval converges to a maximum of 10, as shown in Fig. 1.13a, which is larger than the previous case, which converged to 8. This is consistent with the experimental observations.

Such a stochastic modeling has also been applied in analyzing the morphology of a solar cell that exhibits photosensitivity below the bandgap energy made by an optical near-field assisted method [31].

Furthermore, mathematical modeling helped to unveil the mechanisms of light-assisted surface flattening [35]. More specifically, a two-dimensional hierarchical surface roughness measure taking account of the hierarchical property of optical near-fields was developed and was found to be useful in a demonstration of light-assisted surface processing [99]. As such, system-oriented research will contribute to realizing “nanointelligence” in material applications.

1.5 Conclusion and Future Prospect

In this chapter, we have discussed nanophotonics from the standpoint of information, toward achieving intelligent functions, or what we call “nanointelligence”. In particular, we highlighted optical excitation transfer involving optical near-field

interactions keeping an eye on the possibility of going beyond von Neumann' computing. Nanophotonic security is also presented both theoretically and experimentally. Finally, stochastic modeling, as well as its contribution to material applications, was discussed.

Finally, we make a few remarks on the future prospects of research and development in nanophotonics from an information physics, or system-level viewpoint. We consider that future research and development will be roughly grouped into three categories. The first category concerns further investigation of basic and emergent properties in nanophotonics. For example, scalability and suitable information representations for nanophotonic systems should be further investigated in the future. The second category involves design-related concerns. This chapter mainly exploited optical energy transfer and multipole attributes offered by near-field interactions. The degrees-of-freedom available on the nanoscale, however, are in fact much more abundant and should be thoroughly investigated; these include magnetic field, electron spin, and so on. For instance, magnet-chiral effects [97], energy transfer in diluted magnet semiconductors [62], etc. suggest the importance of including a discussion of spin in the treatment of optical near-fields. In addition, morphology in nanoscale material enables interesting functions, such as light emission from indirect-type semiconductors (e.g., silicon) [15]. It has been suggested that coherent coupling between phonons and optical near-fields lies behind such phenomena [98]. Rigorous theoretical schemes, including ones that offer systematic design frameworks for realizing versatile materials and functionalities, should be investigated. The third category concerns applications; socially and industrially important applications will be pursued in the future [6, 7], and "intelligent" attributes will be one area where the work described in this chapter will contribute.

Finally, we hope that this chapter will contribute to stimulating research in the cross-disciplinary areas of nanophotonics, information, and materials, from fundamental principles to practical applications.

Acknowledgments The authors would like to thank many collaborators for illuminating discussions over several years, in particular H. Hori, T. Kawazoe, T. Yatsui, W. Nomura, K. Kobayashi, K. Akahane, N. Yamamoto, T. Inoue, F. Peper, K. Leibnitz, M. Hoga, Y. Ohyagi, T. Matsumoto, L. B. Kish, C. Lienau, E. Runge, S. Huant, and S.-J. Kim. This work was supported in part by Grants-in-Aid for Scientific Research from the Japan Society for the Promotion of Science (JSPS) and the Strategic Information and Communications R&D Promotion Programme (SCOPE) of the Ministry of Internal Affairs and Communications.

References

1. R.S. Tucker, R. Parthiban, J. Baliga, K. Hinton, R.W.A. Ayre, W.V. Sorin, J. Lightwave Technol. **27**, 243 (2009)
2. T. Ryhänen, M.A. Uusitalo, O. Ikkala, A. Kärkkäinen, *Nanotechnologies for Future Mobile Devices* (Cambridge University Press, Cambridge, 2010)
3. M. Naruse, N. Tate, M. Ohtsu, J. Optics **14**, 094002 (2012)
4. B. Javidi, *Optical and Digital Techniques for Information Security* (Springer, New York, 2005)

5. M. Ohtsu, K. Kobayashi, T. Kawazoe, S. Sangu, T. Yatsui, *IEEE J. Sel. Top. Quantum Electron* **8**, 839 (2002)
6. National Research Council, *Nanophotonics: Accessibility and Applicability* (National Academies Press, Washington, D.C., 2008)
7. MONA (Merging Optics and Nanotechnologies Association) consortium 2008 *A European roadmap for photonics and nanotechnologies*
8. M. Ohtsu, H. Hori, *Near-Field Nano-Optics* (Kluwer Academic/Plenum Publishers, New York, 1999)
9. D.W. Pohl, D. Courjon (eds.), *Near Field Optics* (Kluwer Academic, Dordrecht, 1993)
10. M. Ohtsu, K. Kobayashi, H. Ito, G.H. Lee, *Proc. IEEE* **88**, 1499 (2000)
11. M. Ohtsu, T. Kawazoe, T. Yatsui, M. Naruse, *IEEE J. Sel. Top. Quantum Electron.* **14**, 1404 (2008)
12. M. Ohtsu, K. Kobayashi, T. Kawazoe, T. Yatsui, M. Naruse, *Principles of Nanophotonics* (Taylor and Francis, Boca Raton, 2008)
13. T. Kawazoe, K. Kobayashi, M. Ohtsu, *Appl. Phys. Lett.* **86**, 103102 (2005)
14. H. Fujiwara, T. Kawazoe, M. Ohtsu, *Appl. Phys. B* **98**, 283 (2010)
15. T. Kawazoe, M.A. Mueed, M. Ohtsu, *Appl. Phys. B* **104**, 747 (2011)
16. T. Kawazoe, M. Ohtsu, K. Akahane, N. Yamamoto, *Appl. Phys. B* **107**, 659 (2012)
17. S. Yukutake, T. Kawazoe, T. Yatsui, W. Nomura, K. Kitamura, M. Ohtsu, *Appl. Phys. B* **99**, 415 (2010)
18. M. Aeschlimann, M. Bauer, D. Bayer, T. Brixner, F.A. Javier, W. Pfeiffer, M. Rohmer, C. Spindler, F. Steeb, *Nature* **446**, 301 (2007)
19. T. Kawazoe, M. Ohtsu, S. Aso, Y. Sawado, Y. Hosoda, K. Yoshizawa, K. Akahane, N. Yamamoto, M. Naruse, *Appl. Phys. B* **103**, 537 (2011)
20. T. Yatsui, S. Sangu, T. Kawazoe, M. Ohtsu, S.J. An, J. Yoo, G.-C. Yi, *Appl. Phys. Lett.* **90**, 223110 (2007)
21. N. Tate, H. Sugiyama, M. Naruse, W. Nomura, T. Yatsui, T. Kawazoe, M. Ohtsu, *Opt. Express* **17**, 11113 (2009)
22. N. Tate, M. Naruse, T. Yatsui, T. Kawazoe, M. Hoga, Y. Ohyagi, T. Fukuyama, M. Kitamura, M. Ohtsu, *Opt. Express* **18**, 7497 (2010)
23. A. Drezet, C. Genet, J.-Y. Lalueze, T.W. Ebbesen, *Opt. Express* **16**, 12559 (2008)
24. M. Naruse, T. Kawazoe, R. Ohta, W. Nomura, M. Ohtsu, *Phys. Rev. B* **80**, 125325 (2009)
25. M. Naruse, T. Yatsui, H. Hori, K. Kitamura, M. Ohtsu, *Opt. Express* **15**, 11790 (2007)
26. C. Pistol, C. Dwyer, A.R. Lebeck, *IEEE Micro* **28**, 7 (2008)
27. C. Pistol, W. Chongchitmate, C. Dwyer, A.R. Lebeck, *IEEE Micro* **30**, 110 (2010)
28. P.B. Catrysse, S. Fan, *Nano Lett.* **10**, 2944 (2010)
29. N.G. Van Kampen (ed.), *Stochastic Processes in Physics and Chemistry* (Elsevier, Amsterdam, 2007)
30. P. Bak, C. Tang, K. Wiesenfeld, *Phys. Rev. A* **38**, 364 (1988)
31. M. Naruse, T. Kawazoe, T. Yatsui, N. Tate, M. Ohtsu, *Appl. Phys. B* **105**, 185 (2011)
32. M. Naruse, Y. Liu, W. Nomura, T. Yatsui, M. Aida, L.B. Kish, M. Ohtsu, *Appl. Phys. Lett.* **100**, 193106 (2012)
33. Y. Liu, T. Morishima, T. Yatsui, T. Kawazoe, M. Ohtsu, *Nanotechnology* **22**, 215605 (2011)
34. T. Yatsui, W. Nomura, M. Ohtsu, *Nano Lett.* **5**, 2548 (2005)
35. T. Yatsui, K. Hirata, W. Nomura, Y. Tabata, M. Ohtsu, *Appl. Phys. B.* **93**, 55 (2008)
36. T. Förster, *Ann. Phys.* **2**, 55 (1948)
37. S.A. Crooker, J.A. Hollingsworth, S. Tretiak, V.I. Klimov, *Phys. Rev. Lett.* **89**, 186802 (2002)
38. G.D. Scholes, G.R. Fleming, *J. Phys. Chem. B* **104**, 1854 (2000)
39. M. Kubo, Y. Mori, M. Otani, M. Murakami, Y. Ishibashi, M. Yasuda, K. Hosomizu, H. Miyasaka, H. Imahori, S. Nakashima, *J. Phys. Chem. A* **111**, 5136 (2007)
40. H. Tamura, J.-M. Mallet, M. Oheim, I. Burghardt, *J. Phys. Chem. C* **113**, 7548 (2009)
41. S. Sangu, K. Kobayashi, A. Shojiguchi, T. Kawazoe, M. Ohtsu, *J. Appl. Phys.* **93**, 2937 (2003)
42. T. Kawazoe, K. Kobayashi, J. Lim, Y. Narita, M. Ohtsu, *Phys. Rev. Lett.* **88**, 067404 (2002)
43. T. Itoh, M. Furumiya, T. Ikehara, C. Gourdon, *Solid State Commun.* **73**, 271 (1990)

44. H.J. Carmichael, *Statistical Methods in Quantum Optics I* (Springer-Verlag, Berlin, 1999)
45. X. Wang, N. Wada, *Opt. Express* **15**, 7319 (2007)
46. J.W. Goodman, *Introduction To Fourier Optics* (Roberts & Company, Colorado, 2004)
47. I. Arsovski, T. Chandler, A. Sheikholeslami, *IEEE J. Solid-State Circuits* **38**, 155 (2003)
48. P.-F. Lin, J.B. Kuo, *IEEE J. Solid-State Circuits* **36**, 666 (2001)
49. M. Naruse, T. Miyazaki, F. Kubota, T. Kawazoe, K. Kobayashi, S. Sangu, M. Ohtsu, *Opt. Lett.* **30**, 201 (2005)
50. T. Kawazoe, K. Kobayashi, S. Sangu, M. Ohtsu, *Appl. Phys. Lett.* **82**, 2957 (2003)
51. K. Akahane, N. Yamamoto, M. Naruse, T. Kawazoe, T. Yatsui, M. Ohtsu, Energy transfer in multi-stacked InAs quantum dots. *Jpn. J. Appl. Phys.* **50**, 04DH05 (2011)
52. A. Shojiguchi, K. Kobayashi, S. Sangu, K. Kitahara, M. Ohtsu, Superradiance and dipole ordering of an N two-level system interacting with optical near fields. *J. Phys. Soc. Jpn.* **72**, 2984–3001 (2003)
53. M. Naruse, H. Hori, K. Kobayashi, T. Kawazoe, M. Ohtsu, Pulsation optical pulsation mechanism based on optical near-field interactions. *Appl. Phys. B* **102**, 717–723 (2011)
54. W. Nomura, T. Yatsui, T. Kawazoe, M. Ohtsu, *J. Nanophoton.* **1**, 011591 (2007)
55. T. Yatsui, H. Jeong, M. Ohtsu, *Appl. Phys. B* **93**, 199 (2008)
56. M. Naruse, H. Hori, K. Kobayashi, P. Holmstrom, L. Thylen, M. Ohtsu, *Opt. Express* **18**, A544 (2010)
57. W. Nomura, T. Yatsui, T. Kawazoe, M. Naruse, M. Ohtsu, *Appl. Phys. B.* **100**, 181 (2010)
58. M. Ohtsu, K. Kobayashi, *Optical Near Fields* (Springer, Berlin, 2004)
59. S. Haykin, *Communication Systems* (John Wiley & Sons, New York, 1983)
60. L.B. Kish, *IEE Proc. Circuits Devices Syst.* **151**, 190 (2004)
61. M. Naruse, T. Kawazoe, S. Sangu, K. Kobayashi, M. Ohtsu, *Opt. Express* **14**, 306 (2006)
62. K. Ohmori, K. Kodama, T. Muranaka, Y. Nabetani, T. Matsumoto, *Phys. Status Solidi C* **7**, 1642 (2010)
63. J. Seufert, G. Bacher, H.J. Schömiß, A. Forchel, L. Hansen, G. Schmidt, K.W. Molenkamp, Spin injection into a single self-assembled quantum dot. *Phys. Rev. B* **69**, 035311 (2004)
64. M. Naruse, P. Holmström, T. Kawazoe, K. Akahane, N. Yamamoto, L. Thylén, M. Ohtsu, *Appl. Phys. Lett.* **100**, 241102 (2012)
65. M. Naruse, M. Aono, S.-J. Kim, T. Kawazoe, W. Nomura, H. Hori, M. Hara, M. Ohtsu, *Phys. Rev. B* **86**, 125407 (2012)
66. M. Aono, M. Hara, K. Aihara, *Commun. ACM* **50**, 69 (2007)
67. M. Aono, L. Zhu, M. Hara, *Int. J. Unconventional Comput.* **7**, 463 (2011)
68. B. Korte, J. Vygen, *Combinatorial Optimization: Theory and Algorithms* (Springer-Verlag, Berlin, 2012)
69. M. Aono, M. Naruse, S.-J. Kim, M. Wakabayashi, H. Hori, M. Ohtsu, M. Hara, *Langmuir* **29**, 7557 (2013)
70. S.-J. Kim, M. Naruse, M. Aono, M. Ohtsu, M. Hara, *Sci. Rep.* **4**, 2370 (2013)
71. R.L. van Renesse, *Optical Document Security* (Artech House, Boston, 2005)
72. M. Naruse, H. Hori, K. Kobayashi, M. Ohtsu, *Opt. Lett.* **32**, 1761 (2007)
73. N. Tate, W. Nomura, T. Yatsui, M. Naruse, M. Ohtsu, *Opt. Express* **16**, 607 (2008)
74. M. Naruse, T. Yatsui, W. Nomura, N. Hirose, M. Ohtsu, *Opt. Express* **13**, 9265 (2005)
75. M. Naruse, T. Yatsui, T. Kawazoe, N. Tate, H. Sugiyama, M. Ohtsu, *Appl. Phys. Exp.* **1**, 112101 (2008)
76. M. Naruse, T. Inoue, H. Hori, *Jpn. J. Appl. Phys.* **46**, 6095 (2007)
77. E. Wolf, M. Nieto-Vesperinas, *J. Opt. Soc. Am. A* **2**, 886 (1985)
78. T. Inoue, H. Hori, Quantum theory of radiation in optical near field based on quantization of evanescent electromagnetic waves using detector mode. in *Progress in Nano-Electro-Optics IV*, ed. by M. Ohtsu (Springer, Berlin, 2005), pp. 127–199
79. S.P. McGrew, Hologram counterfeiting: problems and solutions. *Proc. SPIE* **1210**, 66 (1990)
80. H. Matsumoto, T. Matsumoto, *IPJSJ J.* **44**, 1991 (2003)
81. M. Naruse, T. Yatsui, H. Hori, M. Yasui, M. Ohtsu, *J. Appl. Phys.* **103**, 113525 (2008)
82. <http://www.spotafakephone.com/spot-fake-batteries.cfm>. Cited 5 Feb 2012

83. E. Ozbay, *Science* **311**, 189 (2006)
84. L.A. Sweatlock, S.A. Maier, H.A. Atwater, J.J. Penninkhof, A. Polman, *Phys. Rev. B* **71**, 235408 (2005)
85. T. Ishikawa, S. Kohmoto, K. Asakawa, *Appl. Phys. Lett.* **73**, 1712 (1998)
86. T. Yatsui, T. Kawazoe, M. Ueda, Y. Yamamoto, M. Kourogi, M. Ohtsu, *Appl. Phys. Lett.* **81**, 3651 (2002)
87. T. Torimoto, S. Murakami, M. Sakuraoka, K. Iwasaki, K. Okazaki, T. Shibayama, B. Ohtani, *J. Phys. Chem. B* **110**, 13314 (2006)
88. H. Koyama, N. Koshida, *J. Appl. Phys.* **74**, 6365 (1993)
89. E.A. Meulenkaamp, *J. Phys. Chem. B* **102**, 5566 (1998)
90. S. Besner, A.V. Kabashin, F.M. Winnik, M. Meunier, *Appl. Phys. A* **93**, 955 (2008)
91. H.Z. Wu, D.J. Qiu, Y.J. Cai, X.L. Xu, N.B. Chen, *J. Crystal Growth* **245**, 50 (2002)
92. T. Yatsui, S. Takubo, J. Lim, W. Nomura, M. Kourogi, M. Ohtsu, *Appl. Phys. Lett.* **83**, 1716 (2003)
93. A. Wokaun, J.P. Gordon, P.F. Liao, *Phys. Rev. Lett.* **48**, 957 (1982)
94. G.T. Boyd, T. Rasing, J.R.R. Leite, Y.R. Shen, *Phys. Rev. B* **30**, 519 (1984)
95. J. Bosbach, D. Martin, F. Stietz, T. Wenzel, F. Träger, *Appl. Phys. Lett.* **74**, 2605–2607 (1999)
96. K.F. MacDonald, V.A. Fedotov, S. Pochon, K.J. Ross, G.C. Stevens, N.I. Zheludev, W.S. Brocklesby, V.I. Emel'yanov, *Appl. Phys. Lett.* **80**, 1643 (2002)
97. B.A. van Tiggelen, D. Lacoste, G.L.J.A. Rikken, *Phys. B* **279**, 13 (2000)
98. Y. Tanaka, K. Kobayashi, *Phys. E* **40**, 297 (2007)
99. M. Naruse, T. Yatsui, W. Nomura, T. Kawazoe, M. Aida, M. Ohtsu, *Appl. Phys. Lett.* **102**, 071603 (2013)

Nanophotonic Information Physics

Nanointelligence and Nanophotonic Computing

Naruse, M. (Ed.)

2014, XV, 250 p. 151 illus., 57 illus. in color., Hardcover

ISBN: 978-3-642-40223-4